Weak Cell Analysis and Verification for EV System(WAVES)

Dissertation Submitted to
Visvesvaraya National Institute of Technology, Nagpur
in partial fulfillment of requirements for the award of
the degree

Master of Technology
in
"Integrated Power System"

By

Devang Kubitkar
(MT23IPS005)

Under the Guidance of
Dr. Makarand Sudhakar Ballal

DEPARTMENT OF ELECTRICAL ENGINEERING
Visvesvaraya National Institute of Technology
Nagpur - 440 010 (India)

May 2025

Weak Cell Analysis and Verification for EV System(WAVES)

Dissertation Submitted to
Visvesvaraya National Institute of Technology, Nagpur
in partial fulfillment of requirements for the award of
the degree

Master of Technology
in
"Integrated Power System"

By

Devang Kubitkar
(MT23IPS005)

Under the Guidance of
Dr. Makarand Sudhakar Ballal

DEPARTMENT OF ELECTRICAL ENGINEERING
Visvesvaraya National Institute of Technology
Nagpur - 440 010 (India)

May 2025

© 2019, Visvesvaraya National Institute of Technology, Nagpur All rights reserved.

Department of Electrical Engineering
Visvesvaraya National Institute of Technology, Nagpur

Declaration

I, **Devang Kubitkar**, hereby declare that this project work titled **"Weak Cell Analysis and Verification for EV Systems(WAVES)"** is carried out by me in the Department of Electrical Engineering of Visvesvaraya National Institute of Technology, Nagpur. The work is original and has not been submitted earlier as a whole or in part for the award of any degree/diploma at this or any other Institution/University.

Devang Kubitkar
(MT23IPS005)
Date: May 28, 2025

Certificate

The research titled **"Weak Cell Analysis and Verification for EV Systems (WAVES)"** submitted by **Devang Kubitkar** for the award of the degree of Master of Technology has been carried out under my supervision at the Department of Electrical Engineering, Visvesvaraya National Institute of Technology, Nagpur. The work is comprehensive, complete, and fit for evaluation.

30-5-25

Dr. Makarand S. Ballal
Professor
Department of Electrical Engineering,
VNIT, Nagpur
Date: May 28, 2025

Dr. Bhimrao S. Umre
Professor and Head
Department of Electrical Engineering,
VNIT, Nagpur
Date: May 28, 2025

Non-Plagiarism Certificate

This document certifies that the M.Tech Dissertation titled **"Weak Cell Analysis and Verification for EV Systems(WAVES)"**, submitted by **Devang Kubitkar**, Enrollment No. **MT23IPS005**, College ID No. **30818**, is authentic and not plagiarized from any existing literature. Proper acknowledgment has been provided to the original researchers whenever referenced. The Dissertation has undergone plagiarism detection using **TURNITIN** software, and the level of similarity falls within the acceptable range. A brief summary of the report is provided below.

Thesis

ORIGINALITY REPORT

11%	8%	7%	4%
SIMILARITY INDEX	INTERNET SOURCES	PUBLICATIONS	STUDENT PAPERS

Signature:
Name: **Devang Kubitkar**
Enrollment No.: **MT23IPS005**
Date: May 28, 2025

Signature: 30-5-25
Name of Supervisor: **Dr. Makarand S. Ballal**
Professor
Department of Electrical Engineering,
VNIT, Nagpur
Date: May 28, 2025

Acknowledgment

"The finest task of an Engineer is to survey, to plan, to suggest resources and material, assemble them for the task in hand, implement and produce results"

-Sir Mokshagundam Visvesvaraya

First and foremost, I express my gratitude to God for blessing me with good health throughout this journey. I take this opportunity to extend my heartfelt appreciation to my project supervisor, **Dr. Makarand S. Ballal**, Professor in the Department of Electrical Engineering at VNIT Nagpur, for his invaluable guidance, unwavering motivation, and constant support, which paved the way for the successful completion of this project.

I extend my heartfelt thanks to the members of the project evaluation committee, **Dr. Prakash Kulkarni**, **Dr. Nita Patne**, **Dr. Makarand Lokhande**, **Dr. Arghya Mitra** for their thought-provoking questions, insightful feedback, and words of encouragement. My sincere thanks also go to **Dr. B. S. Umre**, Head of the Department of Electrical Engineering, and **Dr. Premlal Patel**, Director of VNIT Nagpur, for providing us with all the necessary facilities in the Electrical Engineering Department.

I am immensely grateful to **Mr. Sarvesh A. Wakode**, **Mr. Shivpal R. Verma** and **Ms. Rashmi Singh** Research Scholars from the Department of Electrical Engineering at VNIT Nagpur, for their technical support, insightful discussions, and valuable suggestions. Additionally, I extend my gratitude to the entire teaching and non-teaching staff for their unwavering support.

Special thanks are due to **M/s Arise Engineers Pvt. Ltd., Vadodara, Gujarat**, for their generous financial assistance during this industrial research project.

Lastly, I express my heartfelt appreciation to my father- figure uncle **Vikas Aher**, my aunt **Vanita** and my mother **Rita** for their constant mental and financial support and encouragement, which has been my driving force and a source of strength throughout this endeavor.

DEVANG KUBITKAR

ABSTRACT

The rapid adoption of electric vehicles (EVs) has heightened the need for reliable battery management systems (BMS) to ensure safety and performance. A critical challenge is the detection of faulty cells within battery packs, particularly in complex configurations like 6S4P (6 series and 4 parallel). Conventional temperature-based monitoring systems in lithium-ion battery packs typically rely on real-time thermal scanning of all individual cells, significantly increases system complexity, data acquisition time, and computational load—particularly in large battery systems. Moreover, continuous monitoring of every cell can be inefficient and often impractical in real-world applications, where fast and accurate fault identification is critical for safety and performance. This project proposes a novel two-way fault detection technique that combines electrical and thermal diagnostics to efficiently identify weak cell. In the first way, abnormal behavior is localized at the parallel strip level using strip voltage analysis, significantly narrowing down the search space. Second way follows the validation, wherein only the cells within the identified strip are scanned using an infrared camera to detect the precise location weak cell based on its thermal signature. This targeted thermal scanning approach substantially reduces hardware requirements, minimizes data processing overhead, and enables faster, more accurate real-time detection. Experimental results validate the effectiveness of the proposed method, demonstrating its potential to outperform traditional thermal monitoring systems in terms of both speed and reliability, especially in applications such as electric vehicles and energy storage systems.

List of Figures

3.1 LIB pack array structure 23
3.2 Strip 1 analysis when all cells are normal 26
3.3 Row 1 analysis when the cell C_{11} is abnormal 27
3.4 Strip 1 analysis when the cell C_{12} is abnormal 28
3.5 Strip 1 analysis when the cell C_{13} is weak 29
3.6 Strip 1 analysis when the cell C_{14} is weak 29
3.7 Generalised curve of strip voltage with respect to the abnormal cell location 32

4.1 Flowchart describing the proposed methodology 34
4.2 Block diagram of the experimental setup 35
4.3 Experimental test bench 35

5.1 Comparison of row 1 voltages in simulation vs hardware 40
5.2 Comparison of row 2 voltages in simulation vs hardware 40
5.3 Comparison of row 3 voltages in simulation vs hardware 41
5.4 Comparison of row 4 voltages in simulation vs hardware 42

6.1 Typical structure of a scaled down model of a 6S4P LIB 47
6.2 WAVES Setup 48
6.3 Validation by Capacitance method Setup 48

List of Tables

2.1 Comparison of major chemical degradation pathways in Li-ion batteries. 16
2.2 Chemical degradation pathways 17
2.3 Comprehensive Overview of the State of the Art Based on Temperature-Based Monitoring Methods 19

4.1 Charging Unit Specifications 36
4.2 Specifications of Li-Ion Battery Pack 36
4.4 Nickel Strip Specifications 37
4.3 Discharging Unit Specifications 37

5.1 Strip voltages under NCND and Discharging for different weak cell locations 39
5.2 Tabular representation of the validation of hardware results obtained under NCND condition for strips 1, 2, 3 and 4 43
5.3 Change in internal resistance observed for row 1,2 and 3 44

6.1 Thermal and Capacitance validation for weak cell detection 47

Index

ABSTRACT i

1 INTRODUCTION 1

1.1 Background and Motivation 2

1.1.1 Need of Electric Vehicles (EVs) 3

1.1.2 Limitations in the Recent State of the Art 4

1.1.3 Lack of abnormal cell detection methods 5

1.1.4 Industry supported project 6

1.1.5 Importance of Detecting Abnormal Cells in Lithium-Ion Battery Packs 6

1.2 Thesis objective 7

1.3 Contribution of this thesis 7

1.4 Thesis organization 8

2 LITERATURE REVIEW 10

2.1 Introduction 10

2.2 Types of Faults in Li-ion Battery Packs 11

2.2.1 Thermal Faults 11

2.2.2 Electrical Faults 12

2.2.3 Mechanical Faults 13

2.2.4 Chemical Faults 14

2.2.5 Causes of Faults 16

2.2.6 Abnormal Cell Detection 18

3 Problem Statement 22

3.0.1 Mathematical Analysis of the Row Voltage with Respect to the Abnormal Cell Location 25

4 Proposed Methodology 33

5 Simulation and Hardware Results 38

6 WAVES Approach for Weak Cell Location Detection in LIB **45**
6.1 Need of WAVES 45
6.2 Working of WAVES 45
6.3 Validation 46

7 Conclusion and Future Scope **49**
7.1 Future Scope 50

A Code for DFT **60**

List of Abbreviations

EV	Electric Vehicle
LIB	Lithium-Ion Battery
LIC	Lithium-Ion Cell
NMC	Lithium Nickel Magnese Cobalt Oxide
SoC	State of Charge
SoH	State of Health
BMS	Battery Management System
OCV	Open Circuit Voltage
SEI	Solid Electrolyte Interphase
NCND	Neither Charging nor Discharging
IR	Internal Resistance

List of Symbols

Li^+	Lithium Ions
V_{oc}	Open Circuit Voltage
R_{int}	Internal Resistance
R_F	Internal Resistance of a weak cell
R_H	Internal Resistance of a healthy cell
C_{mn}	location of the cell in m^{th} strip and at n^{th} location
V_H	Voltage of a healthy cell
V_F	Voltage of a weak cell
N	Number of cells connected in parallel
M	Number of cells connected in series

Research Paper Publications

1. **Devang Kubitkar**, Makarand S. Ballal, "Real-Time Fault Localization in Li-Ion Battery Packs Using Correlation Analysis of BMS-Acquired Charging and Discharging Data," in *2025 IEEE 4th International Conference on Sustainable Energy and Future Electric Transportation (IEEE SEFET 2025)* (Accepted).

2. **Devang Kubitkar**, Makarand S. Ballal, "Correlation-Based Localized Abnormal Cell Detection in Li-Ion Battery Packs Using BMS-Acquired Data in MATLAB Simulink," in *2025 IEEE 4th International Conference on Sustainable Energy and Future Electric Transportation (IEEE SEFET 2025)* (Accepted).

3. Monu Kumar, **Devang Kubitkar**, Makarand S. Ballal, "Charging Area Based State of Health Estimation of Lithium-Ion Battery Pack for EV Applications," in *2025 IEEE 4th International Conference on Power Electronics Drives and Energy Systems (IEEE PEDES 2024)* (Presented).

4. **Devang Kubitkar**, Twinkle Pattnaik, Makarand S. Ballal, "Weak Cell Analysis and Verification for EV System (WAVES)," *submitted to IEEE Access*, May 2025.

Chapter 1

INTRODUCTION

The automotive sector is experiencing a significant shift with the rapid integration of electric vehicles (EVs), which are emerging as a sustainable substitute for traditional vehicles powered by internal combustion engines. EVs bring numerous benefits, such as lower greenhouse gas emissions, reduced operational expenses, and improved energy efficiency. Central to the functionality of these vehicles is the lithium-ion battery (LIB), which acts as the main energy storage unit for powering electric drive systems. The battery pack plays a pivotal role in determining the EV's efficiency and reliability. Globally, the emphasis on energy conservation and emission reduction has positioned EVs as a key area for innovation and development. Lithium-ion batteries have become the preferred energy storage solution for EVs due to their superior characteristics, including high energy density, minimal memory effect, extended cycle life, and low self-discharge rates. These attributes have led to their widespread adoption in EV powertrains. LIBs have outperformed other battery technologies and are now the standard in electric mobility. Their ability to provide longer driving ranges and faster charging times has greatly influenced the growth of the EV market and enhanced consumer interest. Beyond environmental benefits, they also offer economic advantages, reinforcing their role in transforming the automotive landscape and supporting the shift away from fossil-fuel-based transportation. In addition to their role in portable electronics, lithium-ion batteries have become vital in the transportation sector due to their efficiency, longevity, and rapid charging features. Nevertheless, their performance tends to decline over time due to complex internal chemical reactions and varying environmental conditions. This aging process results in reduced capacity, increased internal resistance, and altered voltage behavior, ultimately affecting the battery's state of health (SoH). To maintain the optimal performance and safety of EVs, it is essential to implement a robust Battery Management System (BMS). This system oversees the monitoring and regulation of the battery's operational parameters, helping to improve performance and extend the battery's service life. Continuous tracking of battery behavior is crucial to prevent malfunctions, op-

timize charging strategies, and ensure the battery functions within safe operational limits. Such proactive battery management is critical for sustaining EV reliability, safety, and efficiency throughout their lifecycle.

1.1 Background and Motivation

Lithium-ion (Li-ion) batteries are widely used in electric vehicles (EVs), portable electronics, and grid storage due to their high energy density and efficiency. However, they are susceptible to various electrical faults that can lead to performance degradation, safety hazards, and catastrophic failures. The rapid growth of electric vehicles (EVs), renewable energy storage systems, and portable electronic devices has driven the widespread adoption of lithium-ion (Li-ion) batteries due to their high energy density, long cycle life, and superior performance. However, ensuring the safety, reliability, and longevity of these batteries remains a significant challenge. Among the most critical concerns is the early detection and identification of abnormal cells within a battery pack, as a single faulty cell can degrade overall performance, reduce the pack's lifespan, and, in extreme cases, lead to thermal runaway and safety hazards.

Battery packs typically consist of multiple cells arranged in series-parallel configurations. In such configurations, the failure or degradation of even one cell—due to overcharging, overheating, manufacturing defects, or aging—can affect the voltage balance, current flow, and thermal behavior of the entire pack. Traditional Battery Management Systems (BMS) often monitor only overall pack parameters or group-level voltages, which may not be sufficient to detect early-stage abnormalities at the cell level.

Early and accurate detection of abnormal cells is thus essential for:

- Preventing catastrophic failures and safety incidents,
- Improving battery pack performance and energy efficiency,
- Enabling predictive maintenance and extending battery life.

The motivation behind this project stems from the need for a cost-effective and practical system that can detect the presence and location of an abnormal cell within a Li-ion battery pack in real time. By leveraging voltage sensing techniques and intelligent algorithms, this project aims to develop a two-stage detection system that first identifies the faulty strip based on voltage imbalance, and then localizes the faulty cell using temperature data. This approach ensures both electrical and thermal validation, increasing detection reliability without relying on expensive instrumentation.

This work aligns with current industrial and academic interests in enhancing the safety and intelligence of battery packs used in electric mobility, grid storage, and high-power applications. It also contributes to the broader goal of making energy storage systems smarter, safer, and more sustainable.

The motivation to undertake this project has been significantly bolstered by generous financial support from M/s Arise Engineers Pvt. Ltd., Vadodara, Gujrat. This backing not only underscores the importance of advancing battery technology but also reflects their commitment to fostering innovation in the field of electric vehicles.

1.1.1 Need of Electric Vehicles (EVs)

Compared to conventional internal combustion engine vehicles (ICEVs), electric vehicles (EVs) have numerous benefits that make the transportation system more effective and sustainable. Here are a few key advantages of driving an electric vehicle [3]:

1. **Environmental Benefits:**
   (a) **Reduced Greenhouse Gas Emissions**: Plug-in vehicles (EVs) that run on renewable energy have zero tailpipe emissions, which contributes to reducing climate change and improving urban air quality.
   (b) **Less Noise Pollution:** Since EVs are quieter than traditional vehicles, they help to improve urban environments' overall quality of life by reducing noise pollution.
   (c) **Energy Efficiency:** Compared to internal combustion engines, electric vehicles are significantly more efficient, which reduces overall energy waste and energy consumption per mile traveled.
2. **Economic Advantages:**
   (a) **Lower operating costs:** Compared to ICE vehicles, EVs require less fuel and maintenance. When considering per-mile costs, electricity is typically less expensive than gasoline or diesel. Additionally, as electric vehicles have fewer moving parts, they require less maintenance and their associated expenses are also lower.
   (b) **Energy Independence:** Countries can improve energy security, resilience, and resilience to disruptions in the oil supply and price fluctuation by decreasing their dependency on imported oil.
3. **Public Health Benefits:**

(a) **Improved Air Quality:** By eliminating tailpipe emissions of pollutants such as nitrogen oxides (NOx), particulate matter (PM), and volatile organic compounds (VOCs), EVs help reduce respiratory illnesses and cardiovascular diseases associated with air pollution.

(b) **Reduced Health Care Costs:** Lower air pollution levels lead to a decrease in several health problems, resulting in reduced healthcare expenditures and improved public health outcomes.

4. **Technological Advancements:**

   (a) **Innovative Features:** EVs often incorporate advanced technologies such as regenerative braking, energy-efficient heating and cooling systems, and smart connectivity features that enhance driving experience and convenience.

   (b) **Battery Technology Improvements:** Rapid advancements in battery technology, including higher energy densities, faster charging capabilities, and longer lifespans, are driving down the cost of EVs and improving their performance and range.

5. **Government Incentives and Policies:**

   (a) **Regulatory Incentives:** Incentives such as tax credits, discounts, subsidies, and preferential policies are provided by governments to encourage the use of electric vehicles and accelerate the transition towards electric mobility.

   (b) **Emissions Regulations:** Incentives such as tax credits, discounts, subsidies, and preferential policies are provided by governments to encourage the use of electric vehicles and accelerate the transition towards electric mobility.

1.1.2 Limitations in the Recent State of the Art

Despite considerable advancements in battery management systems (BMS) and fault detection methodologies for lithium-ion battery packs, several limitations persist in current state-of-the-art approaches for abnormal cell detection:

1. **Lack of Cell-Level Resolution:** Many existing monitoring systems focus on pack- or module-level diagnostics, lacking the granularity to detect faults at the individual cell level.

2. **Dependency on Extensive Sensor Networks:** Accurate thermal or voltage-based fault detection often requires numerous sensors, increasing cost and complexity.

3. **Limited Accuracy in Early Fault Detection:** Threshold-based methods struggle to detect early-stage faults or soft failures.

4. **Inadequate Performance Under Dynamic Conditions:** Many methods fail to perform reliably under variable load and temperature conditions typical in real-world EV operations.

5. **High Computational Overhead:** Impedance-based and model-based methods require significant processing power, which is unsuitable for real-time embedded systems.

6. **Lack of Generalization in ML Models:** Many machine learning models are not transferable across different battery chemistries or configurations due to overfitting on specific datasets.

7. **False Alarms:** Algorithms often suffer from high false positive or negative rates, leading to unreliable detection.

8. **Scalability Issues:** Techniques that work well for small packs do not scale efficiently for high-capacity EV or ESS systems.

9. **No Unified Framework:** There's a lack of standardized testing procedures, datasets, or metrics, making comparison across methods difficult.

1.1.3 Lack of abnormal cell detection methods

Despite significant progress in battery monitoring technologies, accurately detecting abnormal cells within lithium-ion battery packs remains a challenging task. Most battery management systems (BMS) monitor parameters at the module or pack level, thereby missing early signs of degradation or faults occurring at the individual cell level [1], [2]. Abnormal cells can arise due to internal short circuits, manufacturing inconsistencies, mechanical damage, or aging, which may not immediately reflect in terminal voltage or surface temperature [3], [4]. Threshold-based detection methods often fail to capture these anomalies under varying load and environmental conditions [5]. Data-driven methods, while promising, face issues such as model generalization and dependency on large training datasets [6], [7]. Furthermore, traditional impedance-based techniques can be intrusive, expensive, or slow for real-time applications [8]. As a result, many faults are only identified after substantial

performance degradation or safety risks have emerged [9]. There's a critical need for high-resolution, cell-level diagnostics that are both non-invasive and adaptive to real-world operating scenarios [10], [11]. Without such advancements, the risks of thermal runaway, energy imbalance, and premature failure will persist in large-scale battery deployments [12].

1.1.4 Industry supported project

The industry and Indian government actively support Electric Vehicles (EVs) through various initiatives, incentives, and policies aimed at promoting its adoption and development. The industrial support by **"M/s Arise Engineers Private Limited, Vadodara, Gujarat"** plays a crucial role in the adoption of this project. The industry's primary focus is figuring out the accurate health status of the LIB packs that are being used constantly in EVs.

1.1.5 Importance of Detecting Abnormal Cells in Lithium-Ion Battery Packs

- **Avoidance of Thermal Runaway and Safety Risks:** Early identification of faulty cells helps prevent overheating that can lead to thermal runaway, thereby reducing the risk of fire or explosions.
- **Ensuring Safe Operation:** Detecting abnormal cells enhances the safety of battery operation during both charging and discharging cycles by preventing unsafe conditions.
- **Prolonging Battery Pack Lifespan:** Managing or isolating defective cells slows down the degradation process of the entire battery pack, extending its overall life.
- **Maintaining Uniform Performance:** Faulty cells cause imbalances in voltage and capacity, which can degrade the performance and reliability of the battery system.
- **Facilitating Proactive Maintenance:** Early detection enables predictive maintenance, allowing interventions before faults cause significant damage or downtime.
- **Preventing Sudden Failures:** Abnormal cells may cause abrupt voltage drops or capacity loss, leading to unexpected system failures if not detected in time.

- **Optimizing Charging Processes:** Accurate identification of problematic cells allows battery management systems to adjust charging protocols for improved efficiency and speed.
- **Boosting Battery Reliability:** Continuous monitoring for cell abnormalities increases confidence in battery performance, especially in critical applications like electric vehicles and energy storage.
- **Supporting Warranty and Diagnostics:** Cell-level fault detection assists manufacturers in warranty validation, failure analysis, and design improvements.
- **Reducing Maintenance Costs:** Targeted replacement of defective cells reduces the need to replace entire battery packs, lowering repair expenses.

1.2 Thesis objective

In lithium-ion battery packs, traditional temperature-based monitoring systems usually depend on real-time thermal scanning of every single cell. This greatly increases system complexity, data acquisition time, and computing burden, especially in large battery systems. Furthermore, in real-world applications where prompt and precise problem diagnosis is essential for performance and safety, continuous monitoring of every cell can be ineffective and even impracticable. In order to effectively identify defective cells, this research suggests a novel two-way fault detection method that integrates electrical and thermal diagnostics. First, the search space is greatly reduced by employing strip voltage analysis to locate anomalous behavior at the parallel strip level. Second way follows the validation, wherein only the cells within the identified strip are scanned using an infrared (IR) camera to detect the precise faulty cell based on its thermal signature. This targeted thermal scanning approach substantially reduces hardware requirements, minimizes data processing overhead, and enables faster, more accurate real-time detection.

1.3 Contribution of this thesis

- Developed a sensorless detection model for identifying abnormal cells in lithium-ion battery packs without the need for extensive physical sensors.
- Utilized minimal physical parameters to accurately locate faulty cells, reducing hardware complexity and cost.

- Designed a real-time detection algorithm capable of monitoring battery pack health during operation.
- Validated the proposed sensorless model through experiments on an actual lithium-ion battery pack.
- Demonstrated improved fault detection speed and accuracy compared to traditional sensor-based methods.
- Reduced system intrusiveness by eliminating the need for additional sensor installations on individual cells.
- Provided a practical and scalable approach suitable for commercial battery management systems.
- Addressed challenges related to real-time implementation and noise robustness in battery health monitoring.
- Enabled early detection of abnormal cells to prevent safety hazards and enhance battery lifespan.
- Contributed a comprehensive study on the relationship between minimal measurable parameters and cell abnormalities in battery packs.

1.4 Thesis organization

This thesis primarily focuses on the determination of the State of Health (SoH) of lithium-ion battery (LIB) packs used in electric vehicles (EVs). The organization of the thesis is as follows:

Chapter 1 introduces the background and motivation of the subject, explains the need for EVs, discusses the limitations in recent state-of-the-art technologies, and defines the thesis's purpose and contributions, considering the necessary assumptions.

Chapter 2 focuses on a literature survey, providing a theoretical overview of LIBs and their different types of faults. It also discusses the detailed state of the art on the various recent methods adopted in the identification of the weak cell location and also a comparative study is presented based on temperature monitoring.

Chapter 3 discusses the problem statement containing the detailed mathematical analysis on the effect of weak cell on the overall rating, capacity and the terminal voltage of the LIB.

Chapter 4 discusses the proposed methodology along with the flowchart describing the steps followed during laboratory experiments and also the simulation of the LIB.

Chapter 5 explains the Simulation and hardware results obtained.

Chapter 6 provides an overview of WAVES technology, explaining its functionality, the equipment used, and the results inferred from it.

Chapter 7 concludes the thesis and suggests directions for future work on all the proposed approaches.

The next chapter, Literature Review, focuses on existing literature to identify current research in the field, highlight research gaps, and guide the project's research work by pinpointing areas that require further investigation. This analysis will provide a foundation for the study's objectives and contributions.

Chapter 2

LITERATURE REVIEW

2.1 Introduction

LIB has become indispensable in modern energy storage systems due to their high energy density, long lifespan, and efficiency [13]. Their applications range from consumer electronics to EV and large-scale grid storage systems, making their reliability and safety a critical concern [14]. However, factors such as capacity degradation, thermal runaway, and internal short circuits pose significant challenges to their operational stability [15]. Detecting these anomalies at an early stage is crucial for enhancing battery safety, efficiency, and longevity [16]. Conventional battery health monitoring methods primarily depend on voltage, current, and temperature measurements. However, these techniques often lack the capability to detect early-stage faults or precisely locate defective cells [17]. To overcome these limitations, researchers have turned to advanced data-driven approaches, particularly machine learning (ML), to improve fault detection and state-of-health (SoH) estimation [18]. Machine learning algorithms have shown remarkable potential in identifying patterns and anomalies in battery performance data. By leveraging historical battery behavior, ML models can predict degradation trends, classify abnormal conditions, and detect faulty cells with improved accuracy [19]. Various algorithms, including Random Forest, Support Vector Machines (SVM), Neural Networks, and clustering techniques, have been extensively used for fault diagnosis [20]. Additionally, optimization algorithms such as Genetic Algorithms (GA) and Particle Swarm Optimization (PSO) have been explored to enhance prediction accuracy and computational efficiency [21]. These data-driven approaches, however, require a lot of data to be gathered and must be trained in a variety of scenarios, including intentionally creating errors. Adoption of EV battery packs is complicated by the localized bad cell identification without tagged information since these packs are put together in series and parallel combinations to satisfy the necessary voltage and capacity requirements. Modern battery management systems have made great strides in monitoring voltage and current, balancing cells, and protecting against issues like overvoltage and overcurrent, yet they

still lack thermal monitoring due to their small number of temperature sensors—two at most, by default. Additionally, BMS treats all parallel cells as a single battery and uses cell balancing, which impacts the entire strip and decreases accuracy in locating the abnormal cell with the lowest voltage. Table 2.3 offers a thorough state of the art based on temperature as a monitoring parameter. However, the idea of using expensive temperature sensors or infrared thermography is limited by issues like cost, quantity, and the inability to reach the targeted abnormal cell because it is not possible to collect a large amount of labeled data to feed the algorithms. The necessity to search for the abnormal cell originates from the fact that an weak cell having less voltage due to degraded capacity and increased internal resistance [22]-[23], acts as a burden on other healthy cells, forcing them to discharge current to it and thus degrading their capacity simultaneously causing overheating in itself, which may trigger thermal runaway if not mitigated within time. Therefore an ideal solution is needed, one that minimizes time restrictions and enhances accuracy through more directed localized monitoring with fewer sensors.

2.2 Types of Faults in Li-ion Battery Packs

2.2.1 Thermal Faults

Thermal faults in lithium-ion battery packs represent one of the most critical safety concerns in energy storage systems, often leading to catastrophic failures if not properly managed. These faults primarily stem from excessive heat generation during operation, which can occur due to several mechanisms. During high-rate charging or discharging, Joule heating ($I^2R_{int}t$) becomes significant, where I is the current and R_{int} is the internal resistance of the cell [24]. This heat generation is exacerbated by exothermic side reactions, such as the decomposition of the solid electrolyte interphase (SEI) layer at elevated temperatures ($> 80\,^{\circ}\mathrm{C}$), which follows Arrhenius kinetics [25].

A particularly dangerous phenomenon is thermal runaway, where localized overheating triggers a self-sustaining cycle of exothermic reactions. This process begins with SEI decomposition, followed by reactions between the anode and electrolyte, and ultimately cathode decomposition releasing oxygen [26]. The heat generation rate during thermal runaway can exceed 10°C/s, with temperatures surpassing 800°C in some cases [27]. These conditions are especially prevalent in large battery packs where thermal propagation between cells can create cascading failures.

To mitigate thermal faults, researchers have developed multi-faceted approaches. At the cell level, improvements include thermally stable electrolytes with flame-retardant additives [28] and ceramic-coated separators that prevent internal short

circuits [29]. Pack-level solutions feature advanced thermal management systems, with liquid cooling demonstrating superior heat removal capabilities (up to 50% better than air cooling) for high-power applications [30]. Phase change materials (PCMs) like paraffin wax composites have shown promise in maintaining cell temperatures within safe limits during transient operations [31].

Emerging technologies include embedded fiber-optic sensors for real-time temperature monitoring [32] and machine learning algorithms that predict thermal runaway onset by analyzing voltage and temperature patterns [33]. These innovations, combined with rigorous safety standards for thermal propagation testing [34], are critical for developing safer battery systems for electric vehicles and grid storage applications.

2.2.2 Electrical Faults

Lithium-ion battery packs, while being the cornerstone of modern energy storage systems, are prone to several electrical faults that can compromise their performance and safety. One of the most critical faults is overcharging, which occurs when cells are charged beyond their upper voltage limit, typically above 4.2 V per cell. This condition leads to lithium plating on the anode and decomposition of the electrolyte, resulting in gas generation and potential thermal runaway [35]. Overdischarge, on the other hand, happens when the cell voltage drops below 2.5 V, causing copper dissolution from the current collector and irreversible capacity loss [36]. Both conditions are particularly dangerous in large battery packs where cell-to-cell variations can exacerbate voltage imbalances.

Internal short circuits present another major challenge, often originating from dendrite growth that pierces the separator or mechanical damage to the cell structure. These shorts create localized hot spots due to Joule heating

$$Q = I^2 R t \tag{2.1}$$

which can trigger thermal runaway if not contained [37]. The literature reports that such events are especially catastrophic in high-energy-density cells where the energy release is more violent. Thermal runaway itself follows Arrhenius kinetics

$$k = A e^{-E_a/RT} \tag{2.2}$$

where exothermic reactions between the electrodes and electrolyte create a self-sustaining cycle of heat generation and decomposition.

To mitigate these risks, researchers have developed multi-layered strategies. Battery Management Systems (BMS) now incorporate precise voltage monitoring algorithms to prevent overcharge and overdischarge conditions [38]. For internal shorts,

ceramic-coated separators have shown promise in resisting dendrite penetration, while pressure-sensitive separators that shut down at elevated temperatures provide an additional safety layer. Thermal management systems using phase-change materials or liquid cooling have been effective in suppressing thermal runaway by maintaining cell temperatures below critical thresholds [39]. Recent advances also include current collectors with carbon coatings to prevent corrosion and AI-based SOC balancing algorithms to minimize cell-to-cell variations. These solutions, when combined, create a robust defense against the most common electrical faults in lithium-ion battery packs.

2.2.3 Mechanical Faults

Mechanical faults in lithium-ion battery packs pose significant safety and performance challenges, particularly in applications subject to dynamic loads like electric vehicles and aerospace systems. These faults typically originate from three primary sources: external impact loads, internal swelling stresses, and manufacturing defects. Under crash conditions, the jellyroll structure of cylindrical cells can experience plastic deformation when stresses exceed the yield strength of the casing material ($\sigma_y >$ 200 MPa for steel casings) [40]. This deformation often leads to separator rupture, creating internal short circuits with localized heat generation rates exceeding 10^6 W/m^3 [41].

A less abrupt but equally critical mechanical fault is electrode stack swelling due to lithium plating and SEI growth during cycling. The resultant compressive stresses ($\sigma_c \approx 5 - 20$ MPa) cause progressive delamination of active material from current collectors, increasing interfacial resistance [42]. This degradation mechanism follows a power-law relationship with cycle count

$$R_{int} \propto N^{0.6} \tag{2.3}$$

and accounts for up to 30% of capacity fade in high-energy cells [43]. Manufacturing imperfections like electrode misalignment or uneven separator tension create localized stress concentrations ($K_t > 3$) that accelerate fatigue failure under vibration loads [44].

Mitigation strategies employ multi-scale approaches. At the material level, silicon-graphite composite anodes with buffering architectures reduce swelling-induced stresses by 40-60% compared to pure silicon [45]. Cell designs now incorporate crush-resistant casings with aluminum honeycomb structures that absorb 50% more energy during impacts [46]. Pack-level solutions include viscoelastic damping materials between cells that reduce vibration-induced damage by damping coefficients (ζ) of 0.2-0.4

[47]. Advanced manufacturing techniques like laser ablation for electrode patterning achieve alignment tolerances <10 μm, minimizing stress concentrations [48].

Emerging diagnostic tools include digital image correlation (DIC) systems that map strain fields with 0.01% resolution [49] and piezoelectric sensors embedded in cell stacks to monitor real-time mechanical stresses [50]. These innovations, combined with finite element analysis (FEA) models that predict failure modes at strain rates up to 1000 s^{-1} [51], are driving safer battery pack designs for extreme environments.

2.2.4 Chemical Faults

Chemical degradation pathways in lithium-ion batteries fundamentally limit their lifespan and safety through irreversible reactions between cell components.

2.2.4.1 Major Fault Mechanisms

1.1 SEI Decomposition The most prevalent fault originates from solid electrolyte interphase (SEI) decomposition at elevated temperatures (> 60 °C), where thermal energy overcomes the activation barrier ($E_a > 0.5$ eV) for organic carbonate reduction [52]. This exothermic process follows pseudo-first-order kinetics with rate constant

$$k_{SEI} = Ae^{-E_a/RT} \tag{2.4}$$

It generates gaseous products (e.g., C_2H_4, CO_2) that increase internal pressure by up to 2 MPa in confined cells [53]. The exothermic nature of SEI decomposition can exacerbate thermal runaway by further elevating cell temperatures, especially under abusive conditions.

1.2 Transition Metal (TM) Dissolution The dissolution of transition metals from layered oxide cathodes such as $LiNi_xMn_yCo_zO_2$ (commonly abbreviated as NMC) is known to accelerate under high potentials, particularly above 4.3 V vs. Li^+/Li. This phenomenon is critical for battery degradation and safety, especially under high voltage and elevated temperature conditions.

The rate of metal dissolution can be described by the Tafel equation:

$$i_{\text{diss}} = i_0 \exp\left(\frac{\alpha F \eta}{RT}\right) \tag{2.5}$$

where:

- i_{diss} is the dissolution current density (rate of dissolution),
- i_0 is the exchange current density,

- α is the anodic transfer coefficient,
- η is the overpotential, defined as the difference between the applied electrode potential and the equilibrium potential,
- F is the Faraday constant (96 485 C/mol),
- R is the universal gas constant (8.314 J/(mol · K)),
- T is the absolute temperature in Kelvin.

The Tafel relationship illustrates that the dissolution rate increases exponentially with overpotential. At high charging voltages, the overpotential η becomes significant, leading to a steep increase in i_{diss}, and hence, faster degradation of the cathode material. This is a critical concern for the longevity and thermal stability of lithium-ion batteries, especially those employing high-nickel content cathodes which are more prone to metal leaching. Transition metal dissolution from layered oxide cathodes ($LiNi_xMn_yCo_zO_2$) is critical above 4.3 V vs. Li/Li^+. The dissolution rate follows a Tafel relationship. Cobalt exhibits the highest dissolution current density ($i_0 \approx 1 \times 10^{-6}$ A/cm^2 at 25 °C) [54]. Dissolved metals (Mn^{2+}, Ni^{2+}) migrate to the anode, catalyzing further SEI growth and increasing charge transfer resistance 3–5x after 500 cycles [55].

1.3 Electrolyte Oxidation Electrolyte oxidation at high voltages generates radical species (RO·, ROO·) that propagate chain reactions through the solvent. Linear carbonate oxidation (e.g., EMC) occurs at potentials above 4.5 V with reaction enthalpy $\Delta H_{ox} < -200$ kJ/mol. Fluorinated phosphates (e.g., $LiPF_6$) hydrolyze to form HF even at water levels as low as 10 ppm [56], reducing electrolyte conductivity from 10 mS/cm to <2 mS/cm after aging [57].

2.2.4.2 Mitigation Strategies

- **SEI Stabilization**: LiDFOB and $LiPO_2F_2$ additives form inorganic-rich interphases with 50% lower electronic conductivity ($\sigma_e < 1 \times 10^{-8}$ S/cm) [58].
- **Cathode Protection**: Atomic layer deposition (ALD) of Al_2O_3 coatings (2 nm thick) reduces TM dissolution rates by 90% at 4.5 V [59].
- **Electrolyte Engineering**: Fluorinated solvents (e.g., FEC) increase oxidation stability to 5.2 V while suppressing HF generation [60].

2.2.4.3 Characterization Techniques

- **DEMS**: Differential electrochemical mass spectrometry quantifies gas evolution with 1 nmol/min sensitivity [61].
- **In-situ NMR**: Tracks lithium deposition chemistry at 10 µm resolution [62].
- **ML-Based Modeling**: Machine learning models trained on quantum chemistry datasets predict decomposition pathways [63].

2.2.4.4 Comparative Summary Table

Table 2.1: Comparison of major chemical degradation pathways in Li-ion batteries.

Fault	Trigger	Effect	Kinetics	Consequence
SEI Decomposition	> 60 °C	Gas evolution	$k = Ae^{-E_a/RT}$	Pressure rise, runaway
TM Dissolution	> 4.3 V	SEI contamination	$i = i_0 e^{\alpha \eta F/RT}$	R_{ct} increase
Electrolyte Oxidation	> 4.5 V	Radical formation	$\Delta H < -200\,\text{kJ/mol}$	Conductivity drop

2.2.5 Causes of Faults

2.2.5.1 Electrical Fault Causes

Overcharge and overdischarge primarily stem from **BMS control failures** where voltage thresholds (4.2 V upper, 2.5 V lower) are exceeded due to:

- Sensor drift ($\Delta V > 50\,\text{mV}$ after 1000 cycles)
- Current collector corrosion increasing internal resistance ($R_{int} \propto l^{0.5}$)
- Passive balancing inefficiency ($< 80\%$) energy transfer) in large packs

2.2.5.2 Thermal Fault Causes

Thermal runaway initiates through three coupled mechanisms:

$$\text{Li}_2\text{CO}_3 \xrightarrow{\text{T}} 2\,\text{Li} + \text{CO}_2 + \frac{1}{2}\text{O}_2 \tag{2.6}$$

$\triangle \text{H} = -200\,\text{kJ mol}^{-1}$

- Separator melt temperature ($T_m < 135\,^\circ\text{C}$ for PE)

- Localized heating ($\nabla T > 10\,^{\circ}\mathrm{C/mm}$) from dendrites
- Exothermic cathode decomposition ($LiCoO_2 \longrightarrow Co_3O_4$) at 150 °C

2.2.5.3 Mechanical Fault Causes

Stress generation follows:

$$\sigma = E\alpha\Delta T + \Omega C_{Li} \quad \text{(Where } \Omega = \text{Partial molar volume)} \tag{2.7}$$

Key contributors:

- Anode expansion (300 % for Si vs 10 % graphite)
- Stack pressure variations ($\Delta P > 1\,\mathrm{MPa}$ in pouch cells)
- Vibration-induced fatigue ($N_f < 10^5$ cycles at 50 Hz)

2.2.5.4 Chemical Fault Causes

Table 2.2: Chemical degradation pathways

Process	Condition	Rate
SEI growth	0 V vs Li/Li^+	2 nm/cycle
TM dissolution	4.5 V, 45 °C	1 mg/m^2/day
Electrolyte oxidation	4.8 V	5 $\mu mol/cm^2$

Lithium-ion battery faults arise from complex interactions between electrical, thermal, mechanical, and chemical degradation pathways. The fundamental causes of electrical faults typically originate from battery management system (BMS) failures, where voltage regulation exceeds safe operating windows. During overcharge conditions (>4.2 V/cell), lithium plating occurs when the intercalation rate is surpassed by reduction kinetics, following a Butler-Volmer relationship where the deposition current density (i) scales exponentially with overpotential (η). Overdischarge (<2.5 V/cell) induces copper dissolution from current collectors, with the corrosion rate following Arrhenius kinetics that accelerates by 3× for every 10 °C temperature increase. These electrical faults are exacerbated by cell-to-cell variations in impedance, which can differ by up to 15% in aged packs due to non-uniform aging.

Thermal faults emerge through coupled exothermic reactions that create positive feedback loops. The solid electrolyte interphase (SEI) begins decomposing at 80 °C to 120 °C with an activation energy of 0.8–1.2 eV, generating flammable hydrocarbons and causing the well-known "thermal runaway" phenomenon. This process is

particularly dangerous in high-nickel cathodes ($LiNi_xMn_yCo_zO_2$) where oxygen release occurs at temperatures as low as 150 °C, with reaction enthalpies exceeding 200 kJ mol^{-1}. Localized heating from internal short circuits can create thermal gradients surpassing 10 °C mm^{-1}, rapidly propagating through adjacent cells.

Mechanical degradation stems from both intrinsic material behavior and external factors. Silicon-containing anodes experience 300% volumetric expansion during lithiation, generating stresses up to 1 GPa that fracture active material particles. These stresses follow a modified Hooke's law relationship ($\sigma = E\epsilon + \Omega\Delta c$), where the chemical expansion coefficient (Ω) dominates at high states of charge. Vibration-induced fatigue in vehicle applications follows a power-law relationship with cycle count ($N_f \propto \epsilon^{-3}$), causing electrode delamination after approximately 100 000 km of driving.

Chemical degradation proceeds through multiple parallel pathways. Transition metal dissolution from cathodes follows a Tafel relationship with dissolution currents reaching 1 µA cm^{-2} at 4.5 V vs. Li/Li$^+$. The resulting metal ions (Mn^{2+}, Ni^{2+}) migrate and deposit on anodes, catalyzing further SEI growth and increasing charge transfer resistance by 3–5×. Electrolyte oxidation at high potentials (>4.8 V) generates radical species that propagate chain reactions, with the oxidation rate increasing tenfold for every 0.5 V potential rise.

Mitigation strategies employ multi-scale approaches. Advanced BMS algorithms using adaptive Kalman filters reduce SOC estimation errors to <2%, while hybrid phase-change thermal management systems maintain temperature variations below 5 °C. Mechanically graded electrodes with spatially varying Young's modulus (50 GPa to 10 GPa gradients) reduce stress concentrations by 60%. Chemically, novel electrolyte formulations incorporating lithium difluorophosphate ($LiPO_2F_2$) additives form stable interphases that reduce gas generation by 80% during high-voltage operation. These solutions, combined with machine learning-based early warning systems detecting subtle impedance changes, are pushing the boundaries of battery safety and reliability.

2.2.6 Abnormal Cell Detection

Table 2.3 provides a comparative overview of several state-of-the-art temperature-based monitoring methods for battery fault detection. Each approach is assessed in terms of its methodology, unique features, benefits, and limitations. Notably, the proposed two-stage method demonstrates enhanced scalability and practicality for real-time diagnosis in large-scale battery systems.

The state-of-the-art in fault detection for LIB in EV showcases advancements

Table 2.3: Comprehensive Overview of the State of the Art Based on Temperature-Based Monitoring Methods

Ref	Methodology	Key Features	Merits	Demerits
[64]	Deep learning-based fault localization using Mask R-CNN on thermal images	Intelligent image processing, location-specific fault detection	High accuracy, real-time detection, suitable for large battery packs	Requires high-quality thermal imaging, computationally intensive
[65]	Data-driven thermal anomaly detection using PCA and control charts	Combines temperature and voltage data	Simple implementation, interpretable results	Limited scalability, prone to false alarms in noisy environments
[66]	Temperature and voltage-based thresholding for anomaly diagnosis	Uses combined temperature-voltage model with threshold-based rules	Low cost, easy integration into BMS	Less accurate under dynamic load/ambient conditions, may miss early faults
[67]	Kalman filtering for temperature behavior modeling	Model-based SoC and thermal behavior estimation	Robust estimation, handles sensor noise well	Requires precise battery modeling, complex implementation
[68]	Correlation-based detection using temperature data across cells	Statistical correlation analysis of temperature rise patterns	No extra sensors required, works for large packs	May not detect isolated faults, needs baseline data

alongside notable limitations. A switched architecture discussed in [69] uses equivalent cell diagnoses, enabling precise fault isolation. However, its implementation complexity and high computational overhead are significant drawbacks. Advances fault monitoring from detection to quantification, improving diagnostic accuracy is reported in [70]. But it needs extensive computational resources and large datasets for training. The fault detection approach for both new and aged cells in [71], effectively addresses aging effects. It still lacks in real-time applicability and scalability under dynamic environments. A weighted Euclidean distance method is explained in [72] for identifying voltage inconsistencies, offering robust fault identification. It is limited to voltage-based faults and ignoring other fault types. A laboratory diagnostics to real-world applications, enhancing practicality detailed in [73]. It faces challenges in scalability and adaptability to diverse operating conditions. A machine learning technique used for fault detection discussed in [74]. It achieves high accu-

racy. But it requires significant computational power and large training datasets. A machine learning application in [75] is for fault analysis in charging stations, and is providing automated solutions. This is toiling with dynamic and unpredictable fault patterns. Article [76] uses segmented regression for fault detection, balancing simplicity and effectiveness. It performs poorly under dynamic operating conditions. A transferable diagnostic algorithm, enhancing adaptability across cells is examined in [77]. However, it needs further validation in diverse real-world scenarios. The multiple minor anomalies, improving diagnostic granularity investigated in [78]. It increases system complexity and computational demands. An exhaustive review of battery faults and diagnostic techniques addressed in [79]. It gives a comprehensive framework for EV safety. It is lacking in novel methodologies for fault detection. A driving data used for battery pack fault diagnosis detailed in [80]. It gives practicality, but it is facing problems with data variability and noise in dynamic environments. An unsupervised adaptive method in [81] is for fleet battery fault detection. It addresses concept drift in evolving environments. It requires extensive computational resources for real-time implementation. Article [82] integrates level shift anomaly detection for BMS fault diagnosis, improving sensitivity to minor faults. However, it is facing challenges in distinguishing between noise and actual anomalies. Study in [83] focuses on faulty sensor signal reconstruction in battery packs, enhancing data reliability. Its performance gets limited by dependency on sensor accuracy and placement. A data-driven fault tracing method, improving fault localization explained in [84]. It also needs large datasets for training. A partial voltage curves for internal short circuit diagnosis is investigated in [85], offering high accuracy. Its application is limited to voltage-based faults. The faults in parallel battery packs is diagnosed in [86], addressing sensor and internal resistance faults. However, it is lacking scalability for larger configurations. An electrode-parameter-based fault diagnosis and capacity estimation is illustrated in [87], improving diagnostic precision. But, it demands precise parameter measurements. A cloud based anomaly detection and classification system is described in [88]. It enhances scalability. It faces latency and data security challenges. Interpretable full-dimensional statistical analytics for soft short-circuit fault diagnosis is given in [89]. It gives high diagnostic accuracy and interpretability. Its outcome is significantly based on computational resources for real-time implementation. A method based on increment capacity curves for micro-short circuit fault diagnosis in parallel battery modules is described in [90]. It provides precise fault identification. Its application is limited to specific fault types and configurations. An early detection of thermal runaway using commercial diagnostic technologies reported in [91]. It provides safety but facing challenges in integrating these technologies into existing BMS frameworks. Article [92] utilizes relaxation voltage for quantitative di-

agnosis of internal short circuits, improving fault quantification accuracy. However, it requires precise voltage measurements and calibration. Recent advancements in BMS have focused on real-time monitoring of cell parameters such as voltage, current, and temperature. However, detecting faulty cells in LIB remains a significant challenge due to the interdependence of cells and the complexity of fault patterns. Traditional methods, such as threshold-based detection, often fail to identify subtle faults or generate false alarms.

The contributions of this thesis are highlighted as follows:(1) A novel technique is proposed that fits a polynomial to the declining row voltage trend in EV battery packs to isolate potential abnormal rows indicative of degraded or faulty cells.(2) A structured two-stage framework is introduced: electrical diagnosis using voltage deviation and curve fitting, followed by thermal imaging to validate the suspected abnormal cells within the identified row.(3) The proposed methodology is implemented on both MATLAB-based simulations and real hardware tests using a 6S4P Li-ion battery pack, confirming consistent voltage drop and thermal anomaly patterns.(4) Correlation Between Internal Resistance and Temperature: Empirical evidence is presented showing how cells with elevated internal resistance due to aging exhibit sharper voltage drops and higher surface temperatures under load.(5) The method relies on voltage and temperature measurements, avoiding the need for invasive cell-level measurements or costly impedance spectroscopy tools, making it practical for BMS integration.(6) By narrowing down the abnormal row first, the approach significantly reduces computational load and thermal data processing, offering a more targeted and time-efficient diagnostic workflow. (7) A new technology based on this proposed methodology has been developed for the detection of weak cell location.

Chapter 3

Problem Statement

The detection of weak cell in LIB presents a significant challenge due to the intricate electrochemical and electrical interactions within series-parallel configurations. In large-scale battery packs used in EV and energy storage systems, cells are interconnected to achieve the desired voltage and capacity. However, this arrangement introduces complexities in charge balancing, heat dissipation, and internal resistance variations, all of which influence battery performance and safety. One of the primary concerns in such architectures is the fluctuation of internal resistance in individual cells, which exhibits a nonlinear dependence on the SoC and temperature. This variation leads to imbalances in voltage distribution, particularly among parallel-connected cells, where small differences in SoC can drive internal circulating currents. These circulating currents, flowing between cells with different potential levels, contribute to localized heating, accelerating degradation, and increasing the likelihood of thermal runaway—one of the most severe failure modes in LIB. Additionally, prolonged exposure to such imbalances can lead to capacity fade, reduced charge retention, and overall reduced battery lifespan. Traditional BMS rely on voltage, current, and temperature monitoring to assess battery health. However, these conventional techniques often fail to detect early-stage faults or accurately identify the location of an abnormal cell due to the nonlinear and dynamic nature of battery behavior. The difficulty is further exacerbated in series-parallel configurations, where changes in a single cell can propagate throughout the entire pack, making fault localization a challenging task. Moreover, existing diagnostic models struggle to incorporate real-time variations in internal resistance, inter-cell interactions, and degradation patterns, limiting their predictive capabilities. In LIB, individual cells are usually connected in parallel and series to create modules, which are subsequently put together to create full battery packs. A module is made up of several cells connected in a certain configuration; several modules are then combined to provide the required voltage and energy capacity.

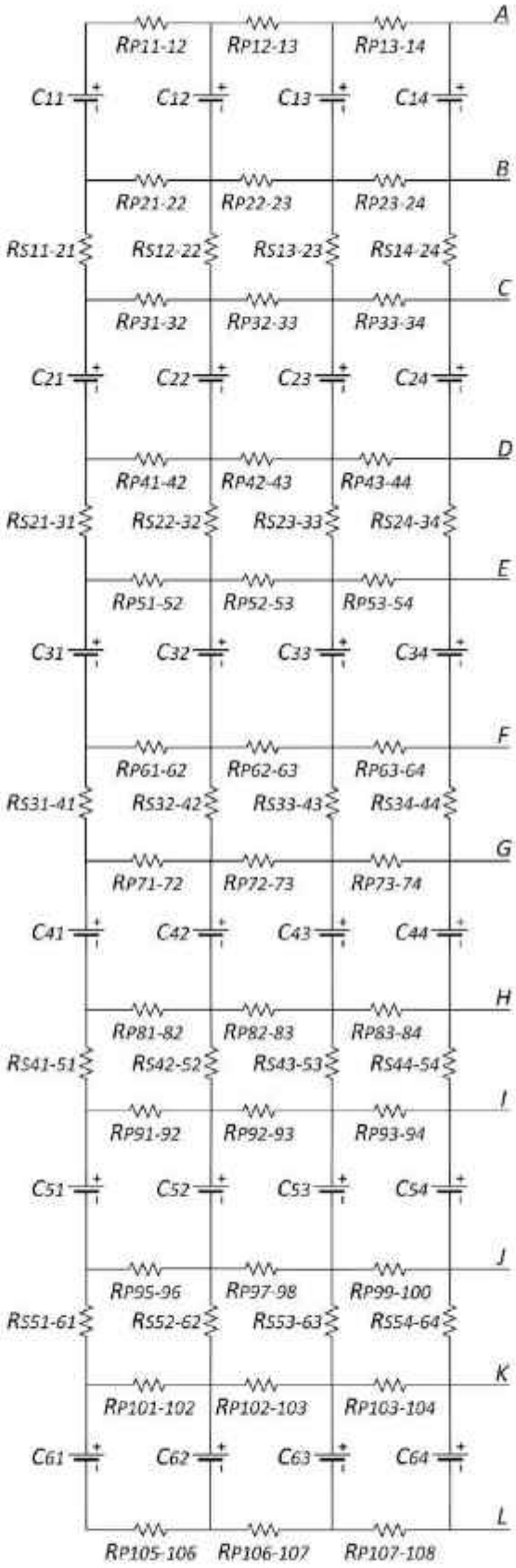

Figure 3.1: LIB pack array structure

Commonly, these configurations are represented by the standard notation $M \times N$, where M is the number of cells connected in series and N is the number of cells connected in parallel. Cells are linked in series by connecting the positive terminal of one cell to the negative terminal of the subsequent cell, producing a cumulative voltage output that satisfies the necessary voltage. When cells are connected in parallel, their separate capacities are combined while the voltage level remains constant, increasing the total capacity. The Ola S1 Pro electric scooter, for instance, comes with two battery options: 3 kWh and 4 kWh. The LIB needed for these variations must be able to deliver a nominal voltage of roughly 51.8 V, which is accomplished by connecting 14 cells in series, each of which has a nominal voltage of 3.7 V. Individual 2.6 Ah cells are connected in parallel, with 10 cells per group, to achieve the necessary energy capacity of roughly 26 Ah. Consequently, a 14S10P battery pack is produced, which offers the voltage and capacity required for the scooter to function. The practical difficulties of handling big battery packs with several series and parallel connections in a lab environment led to the selection of a 6S4P LIB for testing. With a nominal capacity of 10.4 Ah and a nominal voltage of 22.2 V, this arrangement is ideally matched to the capabilities of the charging and discharging devices currently on the market. A summary of the LIB pack's specifications may be found in Table 4.2. Every single cell in the 6S4P arrangement is given a distinct number between 11 and 64, which also serves as a reference to its actual position within the pack. The circuit schematic in Fig. 3.1 depicts this cell mapping. The nickel plates that join cells in parallel inside a strip are represented in this diagram by the horizontally positioned resistors with the labels $R_{P11\text{-}12}, R_{P12\text{-}13}, \ldots, R_{P107\text{-}108}$. It is crucial to remember that the parallel combination of cells is formed by connecting all their positive terminals together and all their negative terminals together, ensuring uniform voltage across the group while increasing the overall capacity. Therefore, six nickel plates per strip are needed to connect four cells in parallel. Similarly, the nickel plates used to connect the cells in series are represented by $R_{S11\text{-}21}, R_{S12\text{-}22}, \ldots, R_{S54\text{-}64}$. Four nickel plates are required to connect any two neighboring strips in series. In this study, the cells connected in parallel are treated as a single unit, referred to as a **"Strip"** or **"Row"**. Consequently, the experimental LIB consists of six such strips connected in series, forming a 6S4P configuration. A BMS is an advanced electronic system that monitors and controls a battery pack, arranged in an array structure, to deliver optimal voltage and current. It ensures safety, protection, cell balancing, state monitoring, thermal regulation, data acquisition, and energy management, enhancing performance and longevity under various operating conditions. A BMS prevents deep discharge and overvoltage caused by rapid charging or high discharge currents. It balances cells by redistributing energy between high-SOC and low-SOC cells using passive or active

methods, including the switched capacitor technique [96, 97, 98]. The measurable parameters provided by the BMS include the terminal voltage V_t, total input current during charging I_c, discharging or load current I_d, row voltages V_{or}, and the SoC of the LIB. Fig 4.2 shows the connection of BMS with 6S4P experimental battery pack. A major challenge lies in determining the location of a weak cell using only this available data under NCND condition. Identifying a weak cell under these conditions remains a significant challenge. Although the BMS monitors individual cells by treating an entire strip as one single cell assuming that when the cells are connected in parallel, the net equivalent voltage across the strip remains constant for over-voltage and under-voltage conditions. A more critical issue arises when a cell's IR increases and its capacity decreases, resulting in a drop in cell voltage. This leads to a corresponding reduction in the respective strip voltage V_{or}. To counteract this, the BMS uses a passive cell balancing system, which redistributes charge from stronger cells to weaker ones under NCND and charging conditions. This approach attempts to boost the charge of the weak cell and maintain the health of the overall battery pack.

3.0.1 Mathematical Analysis of the Row Voltage with Respect to the Abnormal Cell Location

Let us consider the first row of the LIB as shown in Fig. 3.2 for understanding. The LIB is in the NCND condition, i.e., the load is not connected. The battery cells C_{11}, C_{12}, C_{13}, and C_{14} are each charged to V_H V and the internal resistances during healthy condition is R_H Ω. Since all cells are balanced at V_H V and the passive cell balancing System ensures charge redistribution, no potential difference exists between internodes. Without a potential difference, no current flows through the internode resistances, and hence there are no voltage drops across them. As a result, the terminal voltage remains equal to the cell voltage, i.e., V_H V. The voltage sensor measures the full potential difference between points A and B (V_{AB}), which is simply V_H V. Therefore, the row voltage $V_{or1} = V_H$ V.

In this array layout, if one cell, say C_{mn}, is weak and having IR R_F Ω, where $R_F > R_H$. IR of a cell increases with the aging of the cell, the stronger cells that are connected to it in a strip and have more voltage tend to lose their charge by sending off current to the weak cell since current tends to flow from higher potential to lower potential. In Fig. 3.3, if the cell C_{11} is weak and has higher IR, the charge flows from the stronger cells C_{12}, C_{13}, and C_{14} to the weak cell C_{11}. The passive cell balancing redistributes charge from C_{12}, C_{13}, and C_{14} to C_{11} to restore voltage balance. The balancing typically transfers charge gradually to avoid large current

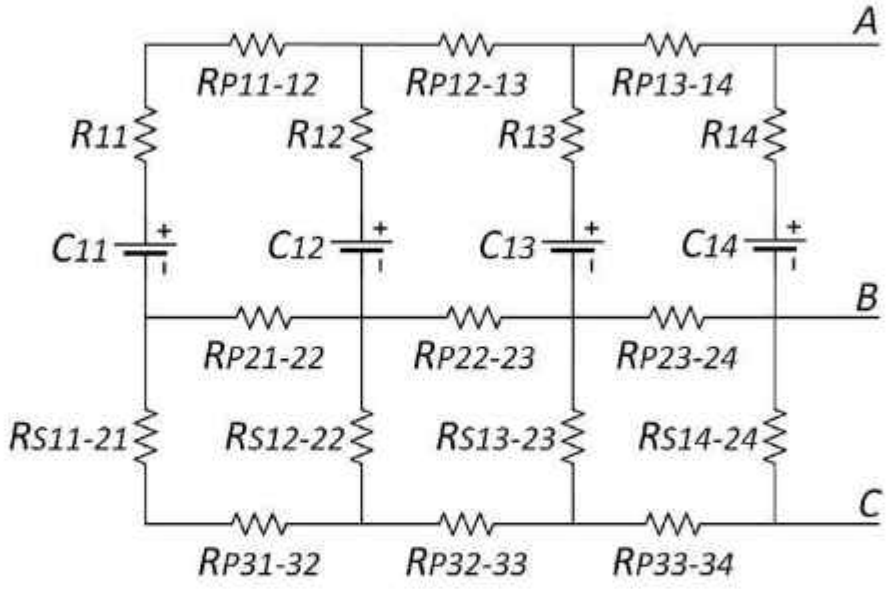

Figure 3.2: Strip 1 analysis when all cells are normal

spikes that could damage the cells. To examine the effect of a weak cell at different locations, an experiment is carried out in the laboratory. The healthy cell at each location is replaced with a weak cell having V_F equal to 3.00 V. When the weak cell having V_F V where $V_H > V_F$ is connected at C_{11} and the rest of the cells are strong at V_H V, charge transfers from C_{12}, C_{13}, and C_{14} to C_{11}. The voltage of C_{11} boosts up to approximately V_{Eq} V, whereas the voltages of cells C_{12}, C_{13}, and C_{14} drop down to approximately V_{Eq} V. The weak cell C_{11} becomes healthy and is continuously fed by the rest of the cells under the NCND condition. Thus, it acts as a load and draws charge or current from the remaining healthy cells.

Case 1 : Cell C_{11} is abnormal

The cell C_{12} is near to C_{11} and feeds energy through path resistance

$$R_{12\text{-}11} = R_{12} + R_{P11\text{-}12} + R_{11} + R_{P21\text{-}22} \tag{3.1}$$

Where $R_{12\text{-}11}$ refers to the resistance path for the current contributed by cell C_{12}, R_{11} and R_{12} represent the internal resistance of the cell C_{11} and C_{12} respectively.

The cell C_{13} feeds energy through path resistance is

$$\begin{aligned} R_{13\text{-}11} = {} & R_{13} + R_{P12\text{-}13} + R_{P11\text{-}12} + R_{11} \\ & + R_{P21\text{-}22} + R_{P22\text{-}23} \end{aligned} \tag{3.2}$$

Where $R_{13\text{-}11}$ refers to the resistance path for the current contributed by cell C_{13}, R_{11} and R_{13} represent the internal resistance of the cell C_{11} and C_{13} respectively.

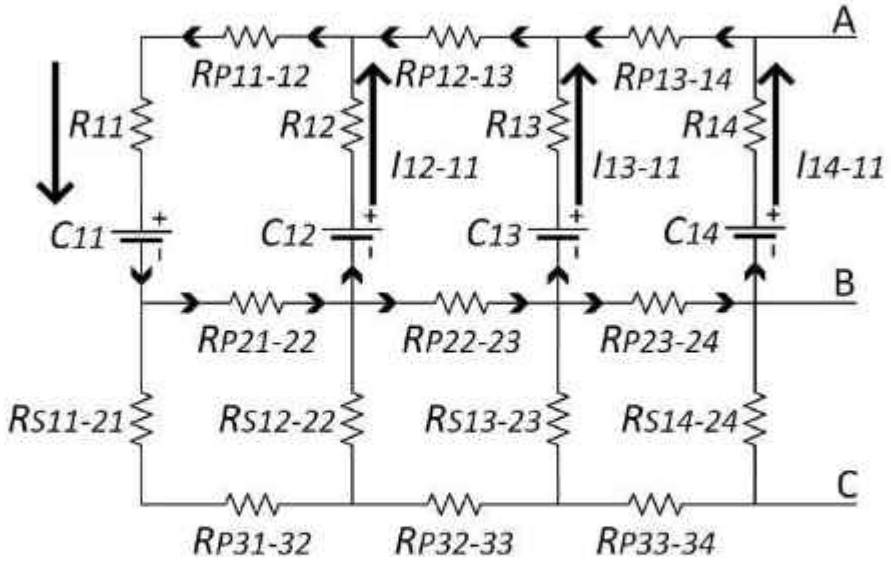

Figure 3.3: Row 1 analysis when the cell C_{11} is abnormal

The cell C_{14} is the farthest from C_{11} and feeds energy through path resistance

$$\begin{aligned} R_{14\text{-}11} &= R_{14} + R_{P13\text{-}14} + R_{P12\text{-}13} + R_{P11\text{-}12} + R_{11} \\ &\quad + R_{P21\text{-}22} + R_{P22\text{-}23} + R_{P23\text{-}24} \\ &= R_{14} + R'_{14\text{-}11} \end{aligned} \tag{3.3}$$

Where $R_{14\text{-}11}$ refers to the resistance path for the current contributed by cell C_{14}, R_{11} and R_{14} represent the internal resistance of the cell C_{11} and C_{14} respectively.

$$\begin{aligned} R'_{14\text{-}11} &= R_{P13\text{-}14} + R_{P12\text{-}13} + R_{P11\text{-}12} + R_{11} \\ &\quad + R_{P21\text{-}22} + R_{P22\text{-}23} + R_{P23\text{-}24} \end{aligned} \tag{3.4}$$

From (3.1), (3.2) and (3.3), we observe that for the condition when C_{11} is weak:

$$R_{12\text{-}11} < R_{13\text{-}11} < R_{14\text{-}11} \tag{3.5}$$

From (3.5), The current provided by the C_{14} is least as compared to the currents contributed by the cells C_{13} and C_{12}. The reason being that the current from the cell C_{14} faces more resistive path and hence its magnitude is the least. Subsequently, the current offered by the cell C_{13} faces more resistive path as compared to the current from the cell C_{12}. This analytically leads to the (3.6). The analytical circuit diagram for this explanation is shown in Fig 3.3

$$I_{12\text{-}11} > I_{13\text{-}11} > I_{14\text{-}11} \tag{3.6}$$

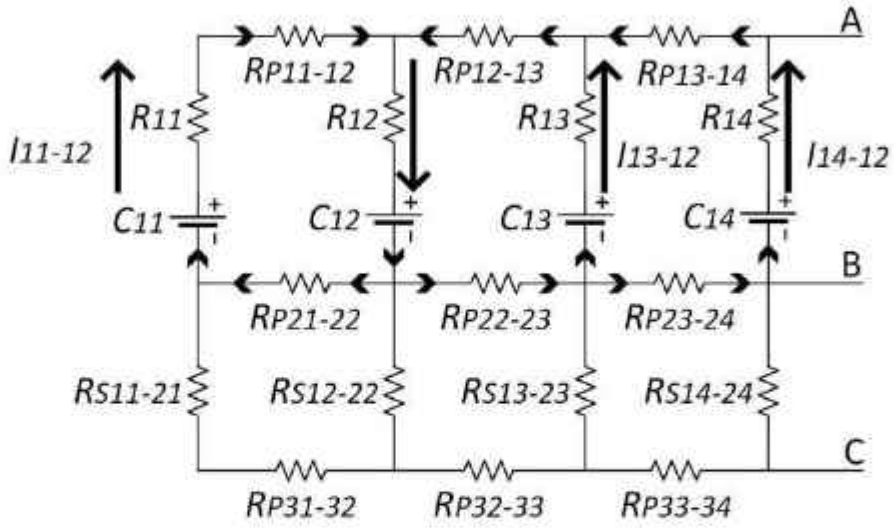

Figure 3.4: Strip 1 analysis when the cell C_{12} is abnormal

In Fig 3.3, $I_{12\text{-}11}$ refers to the current flowing from the cell C_{12} to the cell C_{11}, $I_{13\text{-}11}$ refers to the current flowing from the cell C_{13} to the cell C_{11}, $I_{14\text{-}11}$ refers to the current flowing from the cell C_{14} to the cell C_{11}.

Case 2 : Cell C_{12} is abnormal. The circuit diagram for C_{12} abnormal is shown in 3.4 where $I_{11\text{-}12}$ refers to the current flowing from the cell C_{11} to the cell C_{12}, $I_{13\text{-}12}$ refers to the current flowing from the cell C_{13} to the cell C_{12}, $I_{14\text{-}12}$ refers to the current flowing from the cell C_{14} to the cell C_{12}. The cell C_{11} feeds energy through path resistance:

$$R_{11\text{-}12} = R_{11} + R_{P11\text{-}12} + R_{12} + R_{P21\text{-}22} \tag{3.7}$$

Where $R_{11\text{-}12}$ refers to the resistance path for the current contributed by cell C_{11}.

The cell C_{13} feeds energy through path resistance:

$$R_{13\text{-}12} = R_{13} + R_{P12\text{-}13} + R_{12} + R_{P22\text{-}23} \tag{3.8}$$

Where $R_{13\text{-}12}$ refers to the resistance path for the current contributed by cell C_{13}.

The cell C_{14} feeds energy through path resistance:

$$\begin{aligned} R_{14\text{-}12} &= R_{14} + R_{P13\text{-}14} + R_{P12\text{-}13} + R_{12} \\ &\quad + R_{P22\text{-}23} + R_{P23\text{-}24} \\ &= R_{14} + R'_{14\text{-}12} \end{aligned} \tag{3.9}$$

Where $R_{14\text{-}12}$ refers to the resistance path for the current contributed by cell C_{14}.

$$\begin{aligned} R'_{14\text{-}12} &= R_{P13\text{-}14} + R_{P12\text{-}13} + R_{12} \\ &\quad + R_{P22\text{-}23} + R_{P23\text{-}24} \end{aligned} \tag{3.10}$$

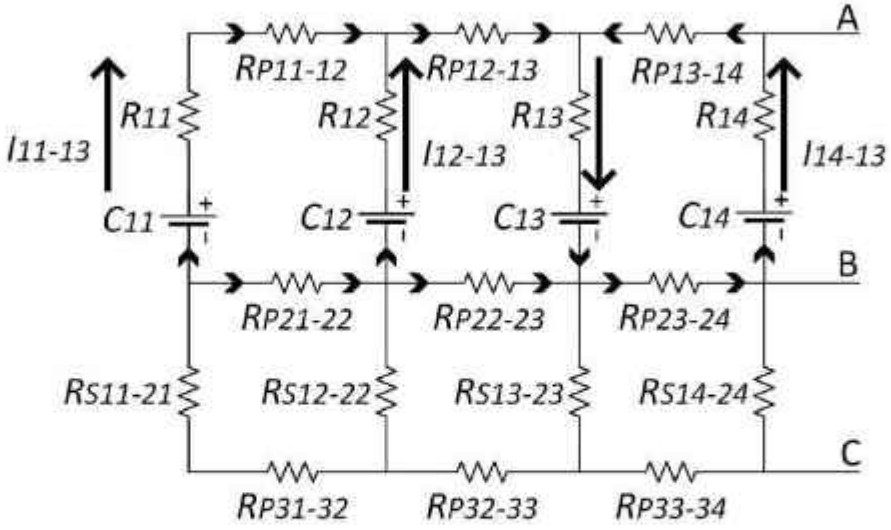

Figure 3.5: Strip 1 analysis when the cell C_{13} is weak

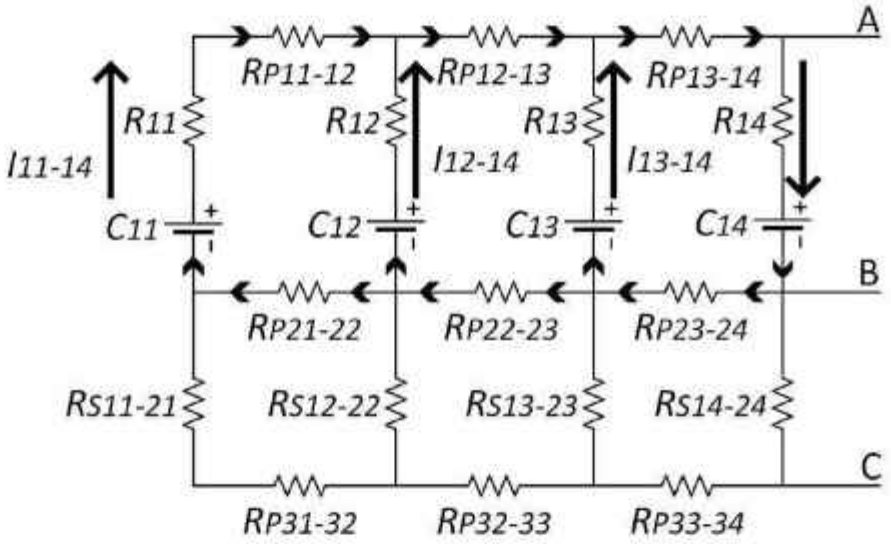

Figure 3.6: Strip 1 analysis when the cell C_{14} is weak

Case 3 : Cell C_{13} is weak. The circuit diagram for C_{13} weak is shown in 3.5 where I_{11-13} refers to the current flowing from the cell C_{11} to the cell C_{13}, I_{12-13} refers to the current flowing from the cell C_{12} to the cell C_{13}, I_{14-13} refers to the current flowing from the cell C_{14} to the cell C_{13}. The cell C_{11} feeds energy through path resistance:

$$R_{11-13} = R_{11} + R_{P11-12} + R_{P12-13} + R_{13} + R_{P22-23} + R_{P21-22} \tag{3.11}$$

Where R_{11-13} refers to the resistance path for the current contributed by cell C_{11}.

The cell C_{12} feeds energy through path resistance:

$$R_{12\text{-}13} = R_{12} + R_{P12\text{-}13} + R_{13} + R_{P22\text{-}23} \tag{3.12}$$

Where $R_{13\text{-}12}$ refers to the resistance path for the current contributed by cell C_{12}.

The cell C_{14} feeds energy through path resistance:

$$\begin{aligned} R_{14\text{-}13} &= R_{14} + R_{P13\text{-}14} + R_{13} + R_{P23\text{-}24} \\ &= R_{14} + R'_{14\text{-}13} \end{aligned} \tag{3.13}$$

Where $R_{14\text{-}13}$ refers to the resistance path for the current contributed by cell C_{14}.

$$R'_{14\text{-}13} = R_{P13\text{-}14} + R_{13} + R_{P23\text{-}24} \tag{3.14}$$

From (3.4),(3.10) and (3.14), we observe that for the condition when C_{12} is weak:

$$R'_{14\text{-}13} < R'_{14\text{-}12} < R'_{14\text{-}11} \tag{3.15}$$

From (3.15), the resistive path for the current coming from the cell C_{14} decreases as the abnormality in the voltage is propagated from the cell C_{11} to the cell C_{14} indicating that the current from the cell C_{14} increases.

$$I_{14\text{-}14} > I_{14\text{-}13} > I_{14\text{-}12} > I_{14\text{-}11} \tag{3.16}$$

Where $I_{14\text{-}14}$ is the current flowing into the cell C_{14} when the cell C_{14} itself was weak, $I_{14\text{-}13}$ is the current flowing from the cell C_{14} when the cell C_{13} was weak, $I_{14\text{-}12}$ is the current flowing from the cell C_{14} when the cell C_{12} was weak, $I_{14\text{-}11}$ is the current flowing from the cell C_{14} when the cell C_{11} was weak.

From (3.16), it can be clearly seen that the current observed flowing through the terminal branch follows an increasing order as the abnormal cell moves its location towards the measuring end i.e towards the terminal AB. In order to obtain the expression for the equivalent row voltage observed across the terminal end AB, we refer Fig 3.3. The row voltage V_{AB11} when the cell C_{11} is weak is given by

$$V_{AB11} = V_{C_{14}} - I_{14\text{-}11} \cdot R_{14} \tag{3.17}$$

The row voltage V_{AB12} when the cell C_{12} is weak is given by

$$V_{AB12} = V_{C_{14}} - I_{14\text{-}12} \cdot R_{14} \tag{3.18}$$

The row voltage V_{AB13} when the cell C_{13} is abnormal is given by

$$V_{AB13} = V_{C_{14}} - I_{14\text{-}13} \cdot R_{14} \tag{3.19}$$

The row voltage V_{AB14} when the cell C_{14} is abnormal is given by

$$V_{AB14} = V_{C_{14}} + I_{14\text{-}14} \cdot R_{14} \tag{3.20}$$

Now $V_{C_{14}} = V_H$ V during healthy condition whereas $V_{C_{14}} = V_F$ V during abnormal condition. Also $R_{14} = R_H$ during healthy condition which is less in magnitude when $R_{14} = R_F$ during abnormal condition. Hence equations (3.17)-(3.20) can be rewritten as follows

$$V_{AB11} = V_H - I_{14\text{-}11} \cdot R_H \tag{3.21}$$

$$V_{AB12} = V_H - I_{14\text{-}12} \cdot R_H \tag{3.22}$$

$$V_{AB13} = V_H - I_{14\text{-}13} \cdot R_H \tag{3.23}$$

$$V_{AB14} = V_F - I_{14\text{-}14} \cdot R_F \tag{3.24}$$

Neglecting the change in internal resistance of the cell C_{14} and applying (3.16), we observe that the row voltage decreases as the abnormality in terms of voltage moves towards the terminal end AB.

$$V_{AB11} > V_{AB12} > V_{AB13} > V_{AB14} \tag{3.25}$$

This relation is observed in both experiment and in simulation as discussed in Section 5. The graphical representation for the above obtained result is shown in the Fig. 3.7. The corresponding polynomial equation constructed for the strip voltage as a function of abnormal cell location, healthy cell voltage, weak cell voltage and the contact resistance is shown below.

$$V_{sp} = \sum_{j=1}^{p} A_j \cdot V_{cj} + B \cdot R \tag{3.26}$$

where p is the number of cells in parallel, indicating that row voltage is dependent on the abnormal cell location, A_j is the coefficient for the j^{th} cell voltage, B is the coefficient for the contact resistance R. s is the strip number. The coefficients are the function of the chemistry of the cells and LIB configuration.

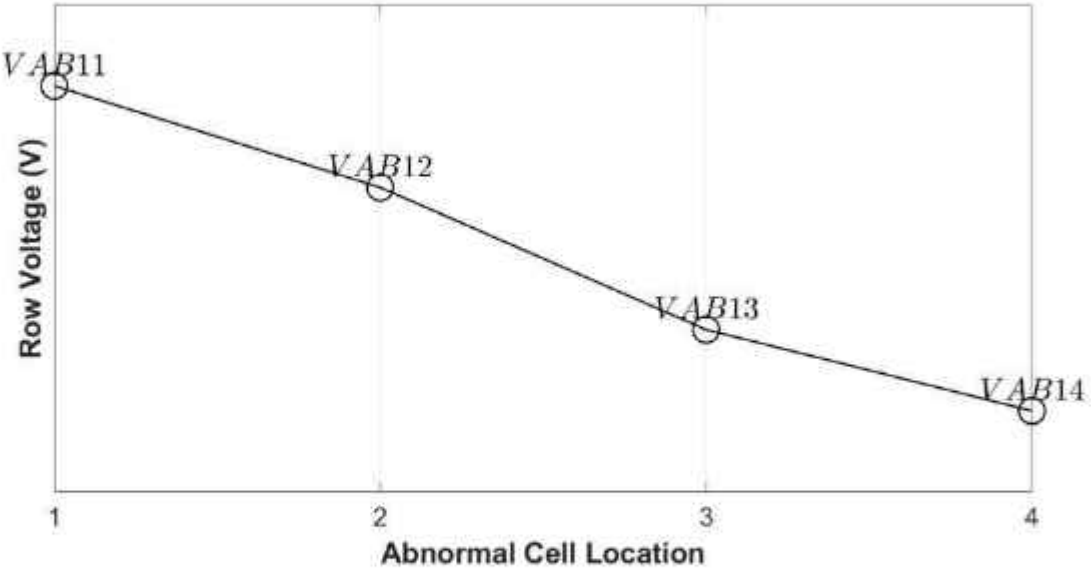

Figure 3.7: Generalised curve of strip voltage with respect to the abnormal cell location

Chapter 4

Proposed Methodology

Based on the proposed expression of (3.26), the proposed methodology is well illustrated in Fig. 4.1. An weak cell having less voltage and more IR is substituted in a certain strip. Although an healthy lithium-ion cell's OCV normally falls between 3.7 V (nominal) and 4.2 V (completely charged), older batteries with higher IR may show lower terminal voltages when under load due to the degradation of active materials and the growth of the SEI layer. In particular, depending on the load and the degree of aging, the voltage may decrease to about 3.0 V or less during discharge. It is crucial to remember that extended use below 3.0 V may result in capacity loss and irreparable damage. The first stage deals with the identification of the abnormal strips having less voltages as compared to other rows or having high voltage differences. The general configuration of an LIB is defined as MSNP. This configuration indicates that the data of 'M' number of row voltages can be obtained. The experimental battery pack considered in this paper for laboratory experiments and *MATLAB* simulation is a 6S4P configuration that provides 6 strip voltages. The experimental test bench is shown in Fig. 4.3. The battery pack is connected to a *JIABADIA* 22S 40 A SMART BMS following the connections shown in the block diagram of Fig. 4.2. The BMS is connected to the host computer via the *UART* cable to proceed with the data acquisition. An auxiliary data acquisition is also possible on a connected mobile device via bluetooth connection. The *Skyrc T*1000 *Charge Maestro* is used to charge or discharge the battery pack. The charging unit is compatible with various battery types such as Li-Ion, Li-Po, Li-Fe, and Li-HV. It can run on both AC and DC supply. Due to the small discharging power limit of this charging unit, an external discharger is needed for discharging the battery pack. The other specifications of this charging unit are described in Table 4.1. The specifications of this discharging unit are given in Table 4.3. The negative power cable from BMS is connected to the negative terminal of the battery pack, whereas the common negative is connected to the negative terminal of the charging/discharging unit as shown in Fig 4.3. The positive terminal of the charging/discharging unit is

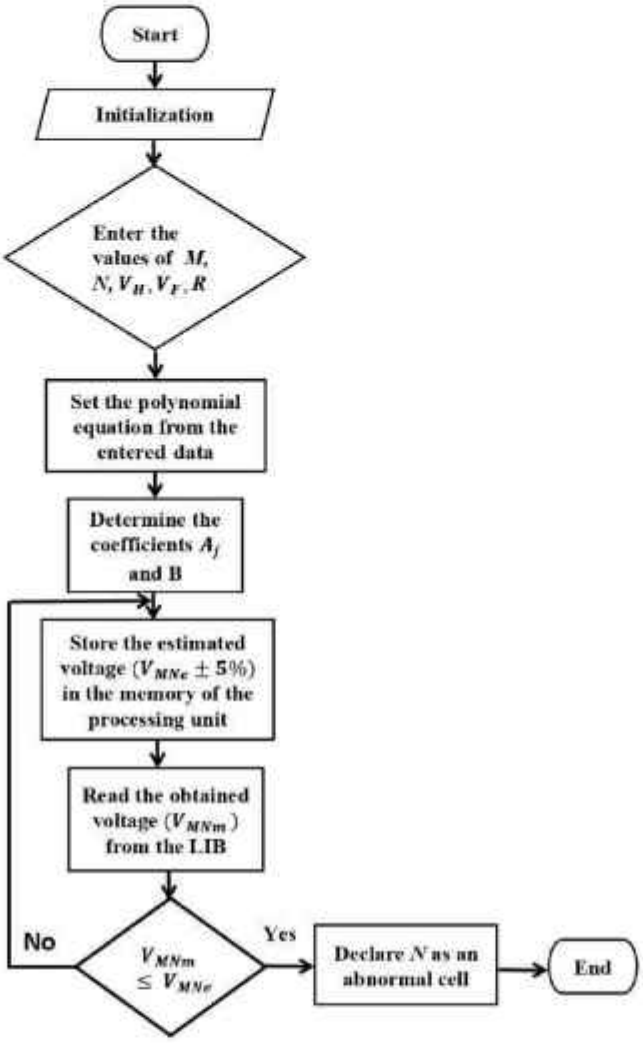
Start
Initialization
Enter the values of M, N, V_H, V_L, R
Set the polynomial equation from the entered data
Determine the coefficients A_j and B
Store the estimated voltage ($V_{MNe} \pm 5\%$) in the memory of the processing unit
Read the obtained voltage (V_{MNm}) from the LIB
No
$V_{MNm} \leq V_{MNe}$
Yes
Declare N as an abnormal cell
End

Figure 4.1: Flowchart describing the proposed methodology

connected to the positive end of the battery pack. During the NCND condition, the charging/discharging unit remains disconnected from the battery pack and BMS. The data is recorded via the $UART$ on the host computer which has six strip voltages, the total voltage of the battery pack, and the discharge current which is constant around 5.2 A. Based on the data of six strip voltages procured, the strip having the least voltage is found to be the abnormal strip which contains the weak cell. So accordingly we obtain a start point strip from where we can start recording the temperature of all cells situated in that abnormal strip thus shifting our targeted focus on that strip

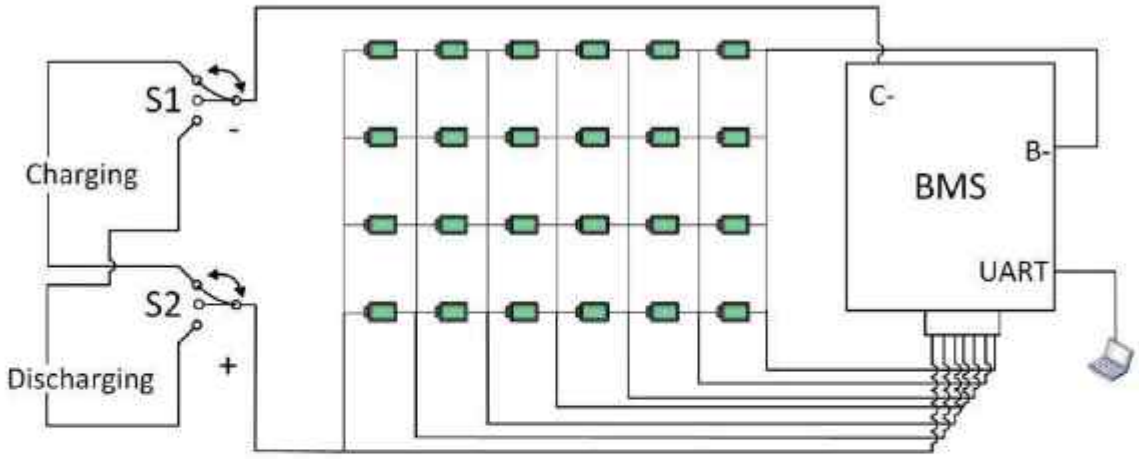

Figure 4.2: Block diagram of the experimental setup

Figure 4.3: Experimental test bench

and also reducing computational data and time. This is the second stage of guided thermal profiling on each cell of only the abnormal strip having the least voltage. The cell in the abnormal row, having the highest temperature is declared as the weak cell.

Additionally, the 6S4P battery pack was simulated in $MATLAB$ using the circuit diagram displayed in Fig 3.1 in order to see the decrease of strip voltages described in (3.25). Based on the data in Table 4.4, the simulation's value for the series and parallel contact resistance is 0.00964 mΩ. The IR of a healthy cell is 30 mΩ, while that of an weak cell is 100mΩ. An healthy cell has a voltage of 4.00 V, while an

weak cell has a voltage of 3.00 V. One cell in each row was rendered weak during the simulation, while the remaining cells remained healthy. In this manner, the weak cell was moved from C_{i1} to C_{i4}, where 'i' represents the i^{th} strip. All six strips whose descriptions are found in Section 5 have their strip voltage data obtained. Although the IR of both cells tends to deviate and thus stays variable, a similar procedure was carried out on a real-time 6S4P battery pack in the lab by substituting the weak cell for the healthy cell in each strip while maintaining the same input parameters as utilized in the simulation. It is important to note that the weak cell voltage does not remain stable at 3.00 V as a result of the inconsistent entropy of the chemical structure within the cell. Consequently, this paper reports the voltages that were defined prior to and following the NCND procedure.

Table 4.1: Charging Unit Specifications

Specifications		**Values**
Input Voltage	AC	100-240 V @ 50 Hz
	DC	10-30 V
Charge Power	AC	450 W max
	DC	1000 W max
Discharge Power	AC	10 W
	DC	350 W
Charge Current		0.1-20 A
Discharge Current	Main Port	0.1-2 A
	External Discharge	0.1-40 A
Battery Configuration		1-6S (Cylindrical Li-Ion)
DC Output	Voltage	5-27 V
	Current	1-15 A

Table 4.2: Specifications of Li-Ion Battery Pack

Parameters	**Specifications**
Battery pack configuration	6S4P
Chemistry type	NMC
Cell model	CMICR18650F8M6-2600mAh
Nominal Capacity	10.4Ah
Nominal Voltage	22.2V
Charging operation	CCCV mode: 24.6 V max, 4.2A charging current, 0.42A end current
Discharging operation	CC mode: 4.2 A discharging current, 18V cut-off voltage
Approx cycle life	600 cycles @ 80% DoD

Table 4.4: Nickel Strip Specifications

Dimension (mm)	**Cell Spacing (mm)**	**Width (mm)**	**Dimension of Square Hole (mm)**
0.15 × 27 × 19.75	19.75	27	12.5 × 12.5

Table 4.3: Discharging Unit Specifications

Specifications	**Values**
Working Voltage	DC 5 V
Discharging Power	350 W
Discharging Current	0.1-40 A
Over Temperature Protection	>95 ^{o}C

The simulation and hardware strip voltage values for different weak cell locations in rows 1 through 4 are graphically compared. To observe the trend of row voltage during discharging, the battery pack undergone a constant 0.5 C rate discharge. The reason behind stressing on discharging, and not on charging, is that the abnormalities show up more during discharge because the battery pack is under load, which causes voltage drops, temperature rise, and resistance effects to become more pronounced which is well studied and mentioned in this study. Weak cell's drop voltage is faster or heats more than healthy ones which are more observable during discharge [93]. Charging hides problems temporarily since a constant current or constant voltage is applied, and cells may look similar if the balancing of the BMS, which offers ON state balancing only for NCND and charging conditions [94]. Again discharging is generally safer than charging when testing for faults because charging may lead a weak cell to overcharge, heat up, and eventually enter thermal runaway [95]. Hence this paper evaluates discharging as the better procedure for weak cell detection at an intermediate C rate to reduce the rapid fluctuations of internal resistance and avoid deep discharge of the abnormal row containing abnormal cells whose probability of happening increases if at all the C rate is kept high.

Chapter 5

Simulation and Hardware Results

The simulation results for NCND condition is shown in the Table 5.1. This infers that the strip voltage tends to decrease with the weak cell location as it moves towards the terminal end, following what was mathematically observed from (3.25). The assumptions followed during the simulation process is that the IR of both the healthy and weak cell is constant however during real time hardware process in laboratory, the variation in the IR is recorded. Also, the voltage, while replacing an healthy cell with a weak cell, is kept constant. The row voltages along with the change in the voltage of individual cell before and after the NCND process is shown in the Table 5.2. The first column in the Table 5.2 represents the strip in which, one by one, each healthy cell is replaced by an weak cell, leading to the voltage drop of that strip. Accordingly, the second column shows the location in that strip where a healthy cell was replaced by a weak cell. For every weak cell, the third column summarizes the status of each cell in that abnormal strip by mentioning 'H' for healthy status and 'F' for weak or faulty status. The fourth column is dedicated to the OCV of each cell before connecting them in parallel in the strip, and the fifth column shows the terminal voltage of each cell after the NCND process. It is observed that the voltage of the weak cell in every case of abnormal strip increases because the other healthy cells support it by transferring charge.

Hence for instance when the cell C_{14} is weak in row 1, the voltages of C_{11},C_{12} and C_{13} before connection were respectively 4.00 V, 4.00 V, 3.99 V which on after connection in parallel, reduced to 3.98 V, 3.99 V and 3.98 V. However, the voltage of the cell C_{14} increases from 3.01 V to 3.77 V. This justifies the statement that healthy cells tend to boost the voltage of the abnormal cell. The sixth column shows the values of the temperature recorded for all cells. A *Fluke* Thermal imaging camera was used to record the temperatures. It is clear from the values that the weak cell has the highest temperature among the others due to the heating caused by the flow of charge from other healthy cells when connected in parallel. The Table 5.2 validates the estimated weak cell location by measuring the temperature.

Table 5.1: Strip voltages under NCND and Discharging for different weak cell locations

Strip	Weak Cell	NCND (V)	Discharging (V)
1	11	3.9449	3.8319
	12	3.9361	3.8157
	13	3.8990	3.7538
	14	3.7854	3.5504
2	21	3.9447	3.8585
	22	3.9360	3.8453
	23	3.8991	3.7918
	24	3.7858	3.6273
3	31	3.9556	3.8651
	32	3.9426	3.8525
	33	3.8952	3.8005
	34	3.7561	3.6412
4	41	3.9152	3.8512
	42	3.9094	3.8325
	43	3.8850	3.7969
	44	3.8240	3.6350

Thus temperature acts as an important parameter which informs about the presence of a weak cell in a row because if any any strip is having an abnormal cell, then definitely the weak cell will act as a load on other cells, drawing more charge towards it and thus getting heated up which eventually creates a localized hotspot. The last column in Table 5.2 represents the strip voltage for the corresponding weak cell. A declining trend for the strip voltage is observed, validating the results obtained in the *MATLAB* simulation during the NCND condition.

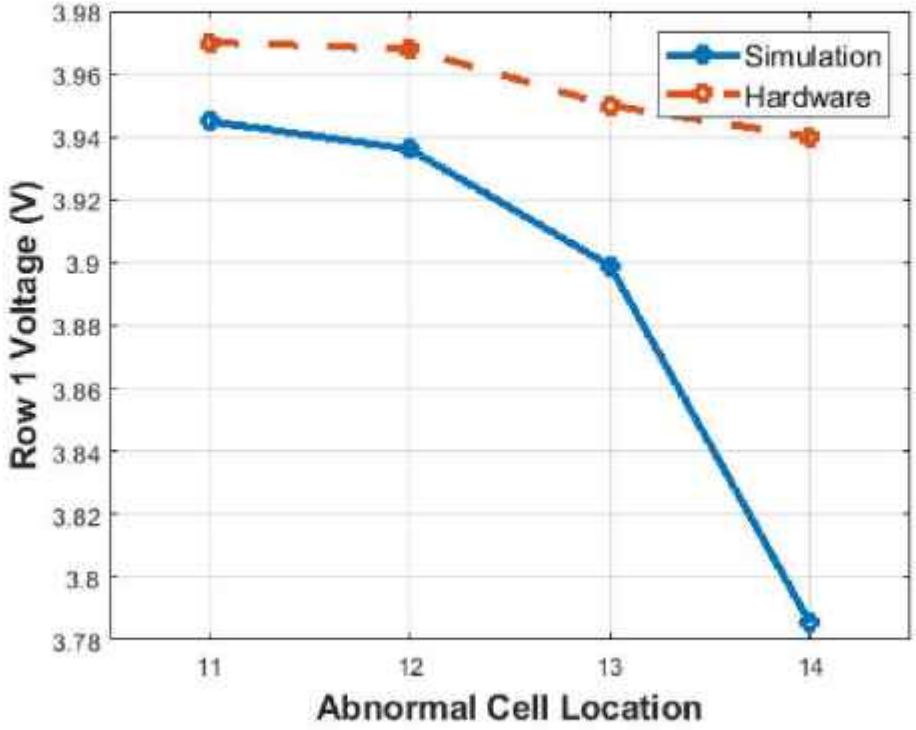

Figure 5.1: Comparison of row 1 voltages in simulation vs hardware

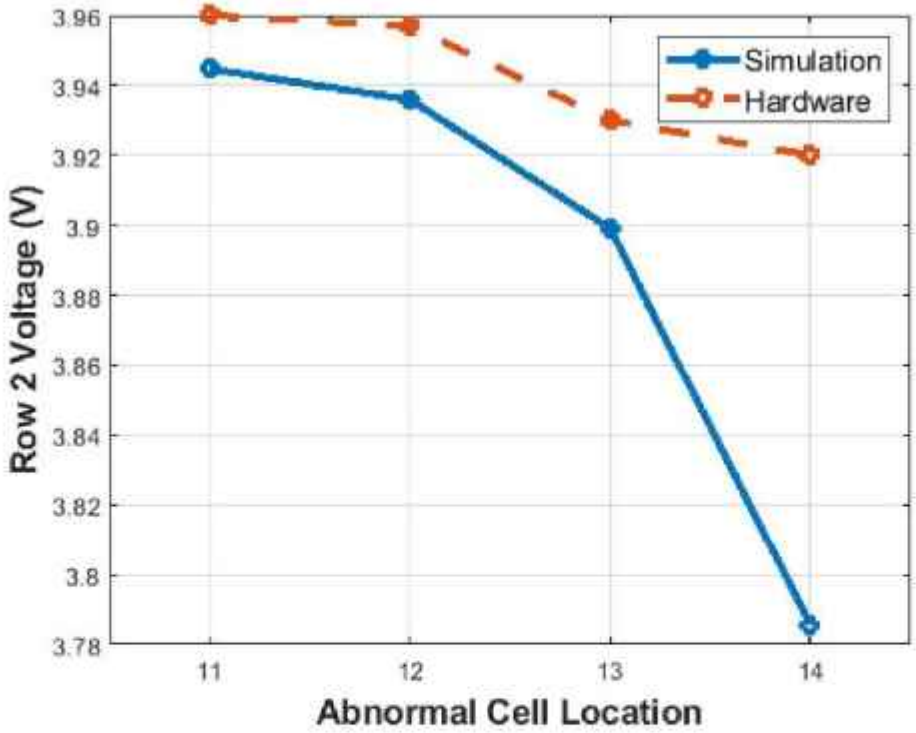

Figure 5.2: Comparison of row 2 voltages in simulation vs hardware

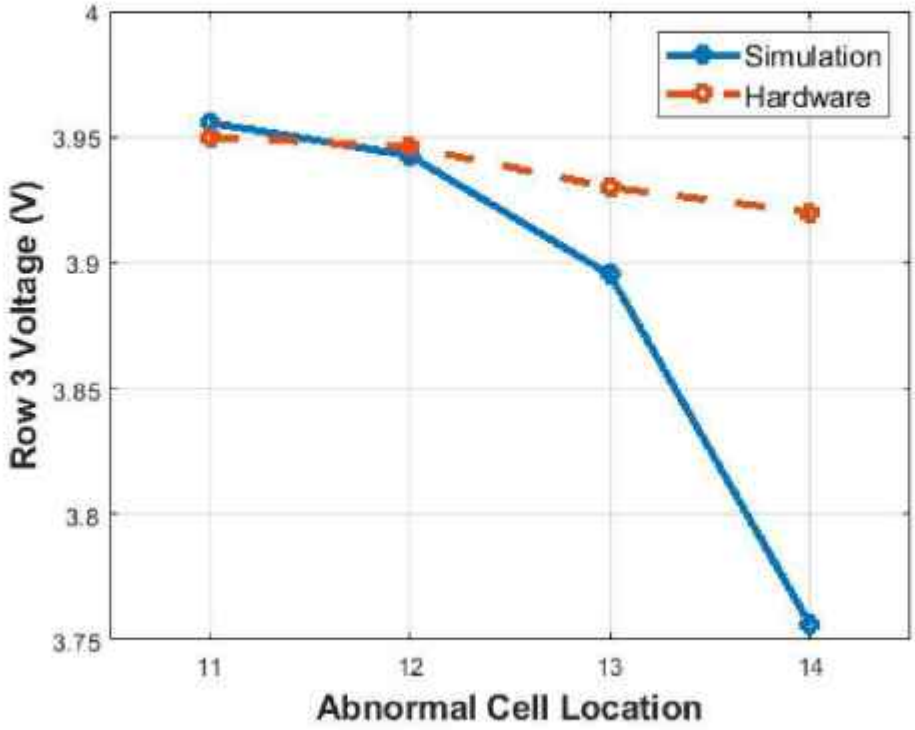

Figure 5.3: Comparison of row 3 voltages in simulation vs hardware

The weak cell detection process begins by iteratively checking each cell, from V_{C1} to V_{C4}. For each iteration, the current cell V_{Ci} is assumed to be the weak cell, and is assigned the voltage V_F V in the right hand side of the equation (3.26), rest all other cell voltages in the equation are replaced with the healthy voltage value V_H V. During laboratory experiment, the respective values values of V_H and V_F at which healthy and weak cells were kept are as follows: $V_H = 4.00$V ; $V_F = 3.00$ V. The value of the contact resistance R substituted as 0.00964mΩ as was calculated from the specifications provided in the Table 4.4. Consequently, in each iteration, the corresponding strip voltage obtained from the hardware results for a certain strip, were substituted in the left hand side of the equation (3.26). After solving the system of equations, the coefficients on the right hand side of the equation (3.26) are estimated which will be used in estimating the strip voltage for a new test case. Based on the data obtained and following the initial expression proposed in (3.26), a polynomial equation is framed as follows

$$V_{MNm} = 0.03 \cdot V_{C1} + 0.04 \cdot V_{C2} + 0.05 \cdot V_{C3} + 0.06 \cdot V_{C4} + 340.249 \cdot R \tag{5.1}$$

.

The result is then compared to the measured or obtained strip voltage. If the

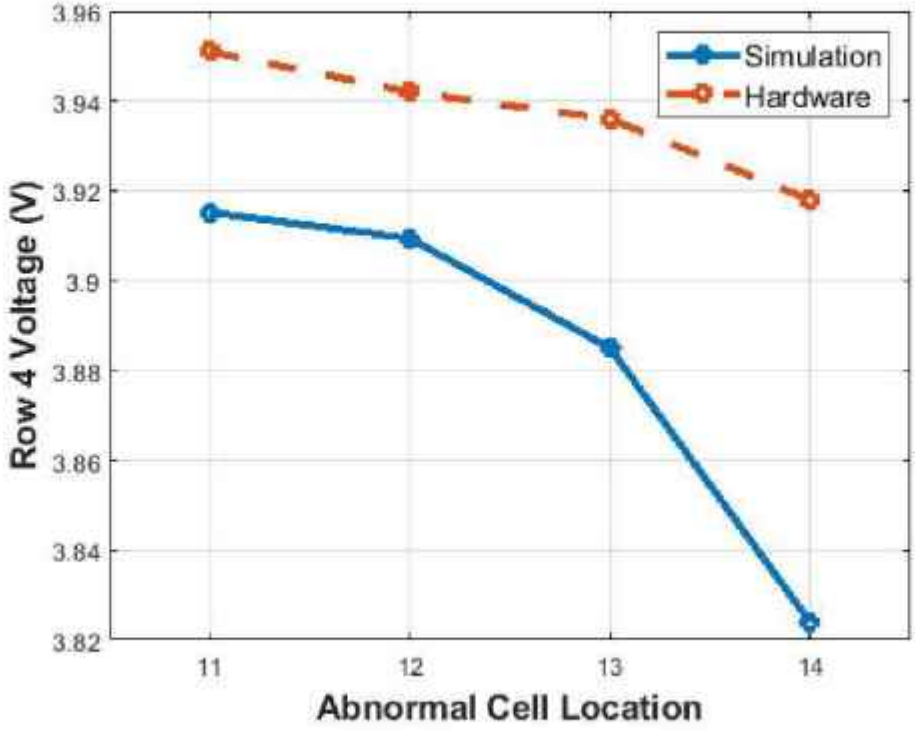

Figure 5.4: Comparison of row 4 voltages in simulation vs hardware

estimated strip voltage lies within the range of $V_{MNm} \pm 5$ mV, then the current cell C_j is identified as the weak cell, and the process is terminated as shown in the Fig. 4.1. If not, the process continues with the next cell in the sequence. This procedure is repeated until a match is found or all cells have been evaluated.

Fig. 5.1, 5.2, 5.3, 5.4, respectively show the comparison between the simulation and hardware results under NCND condition for the strips 1, 2, 3 and 4. The X-axis stands for the different weak cell location following the notations as shown in 3.1 while the Y-axis stands for the strip voltage obtained as output from the experiment for each weak cell location. The strip voltage is seen to follow a decreasing trend both in simulation and hardware process, thus validating the mathematically derived strip voltage decremental curve as was depicted in 3.7. The strip voltage curves obtained as part of hardware outcome do not exactly follow the trend that was observed in the simulation because, practically, the IR tends to vary since it depends on the temperature, state of charge, and the aging of the cell. This change in IR before and after connection in parallel for rows 1,2, and 3 is more precisely shown in the Table 5.3. It is observed that the IR of the weak cell tends to improve, i.e, decrease as its voltage increases since IR follows an inverse non-linear nature with the voltage. Hence, IR is a sharp indicator of the age of a Li-ion battery.

Table 5.2: Tabular representation of the validation of hardware results obtained under NCND condition for strips 1, 2, 3 and 4

Weak Strip	Weak Cell	Cell	Voc (V)	Vt (V)	T (°C)	Vor (V)
1	14	11(H)	4.00	3.98	32.6	3.949
		12(H)	4.00	3.99	32.7	
		13(H)	3.99	3.98	33.0	
		14(F)	3.01	3.77	33.4	
	13	11(H)	4.00	3.99	33.5	3.950
		12(H)	4.00	3.99	32.9	
		13(F)	3.03	3.61	34.5	
		14(H)	4.00	3.99	32.5	
	12	11(H)	4.00	3.98	36.8	3.968
		12(F)	3.04	3.70	38.3	
		13(H)	4.00	3.99	36.6	
		14(H)	3.99	3.98	36.8	
	11	11(F)	3.02	3.78	38.8	3.970
		12(H)	4.00	3.99	37.5	
		13(H)	4.00	3.99	37.5	
		14(H)	4.00	3.99	37.3	
2	24	21(H)	3.99	3.98	36.4	3.929
		22(H)	3.99	3.98	36.1	
		23(H)	3.99	3.98	36.5	
		24(F)	2.99	3.68	40.9	
	23	21(H)	3.99	3.98	36.6	3.930
		22(H)	3.99	3.98	36.2	
		23(F)	3.00	3.67	37.4	
		24(H)	3.99	3.98	36.1	
	22	21(H)	3.99	3.98	37.5	3.957
		22(F)	3.00	3.65	40.7	
		23(H)	3.99	3.98	36.9	
		24(H)	3.99	3.98	37.0	
	21	21(F)	3.00	3.68	41.3	3.960
		22(H)	3.99	3.98	37.2	
		23(H)	3.99	3.98	36.8	
		24(H)	3.99	3.98	36.5	
3	34	31(H)	4.00	3.99	37.0	3.929
		32(H)	4.00	3.99	37.2	
		33(H)	4.00	3.98	35.8	
		34(F)	2.99	3.73	37.8	
	33	31(H)	4.00	3.99	36.7	3.930
		32(H)	4.00	3.98	36.4	
		33(F)	3.02	3.76	37.7	
		34(H)	4.00	3.99	35.9	
	32	31(H)	4.00	3.99	37.4	3.946
		32(F)	3.03	3.56	39.4	
		33(H)	4.00	3.99	37.6	
		34(H)	4.00	3.99	37.6	
	31	31(F)	3.02	3.74	36.6	3.950
		32(H)	4.00	3.98	35.4	
		33(H)	3.99	3.99	35.0	
		34(H)	4.00	3.98	34.9	
4	44	41(H)	4.00	3.99	31.9	3.918
		42(H)	4.00	3.98	32.8	
		43(H)	4.00	3.99	31.7	
		44(F)	3.00	3.72	33.0	
	43	41(H)	3.99	3.99	30.7	3.936
		42(H)	3.99	3.99	30.6	
		43(F)	3.02	3.50	32.2	
		44(H)	4.00	3.99	31.1	
	42	41(H)	4.00	3.99	34.3	3.942
		42(F)	2.99	3.72	34.8	
		43(H)	4.00	3.99	34.2	
		44(H)	4.00	3.99	33.8	
	41	41(F)	3.00	3.68	35.6	3.951
		42(H)	4.00	3.98	34.9	
		43(H)	4.00	3.99	34.5	
		44(H)	4.00	3.98	34.7	

Table 5.3: Change in internal resistance observed for row 1,2 and 3

Weak Row	**Weak Cell**	**Cell**	**IR before connection (mΩ)**	**IR after connection (mΩ)**
1	14	11(H)	48	50
		12(H)	45	68
		13(H)	60	57
		14(F)	341	157
	13	11(H)	32	32
		12(H)	37	39
		13(F)	286	162
		14(H)	42	42
	12	11(H)	49	40
		12(F)	267	142
		13(H)	46	34
		14(H)	36	43
	11	11(F)	281	223
		12(H)	48	33
		13(H)	41	36
		14(H)	43	38
2	24	21(H)	32	30
		22(H)	34	36
		23(H)	33	35
		24(F)	302	150
	23	21(H)	30	32
		22(H)	36	44
		23(F)	275	167
		24(H)	35	33
	22	21(H)	30	29
		22(F)	293	167
		23(H)	36	36
		24(H)	34	35
	21	21(F)	273	146
		22(H)	31	29
		23(H)	34	39
		24(H)	34	33
3	34	31(H)	29	31
		32(H)	31	31
		33(H)	32	33
		34(F)	284	142
	33	31(H)	34	32
		32(H)	32	31
		33(F)	256	145
		34(H)	38	33
	32	31(H)	38	30
		32(F)	238	152
		33(H)	34	33
		34(H)	33	35
	31	31(F)	261	154
		32(H)	32	35
		33(H)	31	33
		34(H)	35	36

Chapter 6

WAVES Approach for Weak Cell Location Detection in LIB

Based on the proposed methodology, as depicted in Fig. 4.1, a technology was developed in the laboratory for the detection of the location of the weak cell in a LIB. "WAVES" stands for weak cell analysis and verification for EV systems. This kit utilizes only strip voltage data, which is fed to its algorithm, and outputs the location of the weak cell. Without the use of much sensors and most importantly without reaching out to each cell, which in turn reduces the computational burden, relying on minimal measurable parameters and includes a strong mathematical foundation as was described in the Section 3.

6.1 Need of WAVES

A weak cell tends to deteriorate the overall rating, capacity and the terminal voltage of the LIB, leading to the improper operation of the appliance connected. Hence, to address this problem, the isolation of this weak cell is very important because there are chances that this weak cell might enter thermal runaway stage, thus damaging the battery.

6.2 Working of WAVES

The developed technology works in three stages. The first stage deals with the data procurement from the LIB using a voltage divider circuit which feeds the data to the micro-controller. The second stage deals with the identification of the weak strip, having the least voltage, which indicates the presence of a weak cell in that strip. Third stage involves the application of the algorithm , inserted in the micro-controller, consisting of the analytical equation that will provide the location of the weak cell. The *WAVES* system is developed for monitoring strip voltages in a lithium-ion battery pack configured in a 6S4P arrangement. The circuit employs six DC voltage sensors, each assigned to monitor a specific strip. These sensors scale

down the high strip voltages—which range from 4 V to 24 V—to levels below 5 V, making them suitable for direct interfacing with the analog input pins of an Arduino micro controller. To accommodate multiple sensor inputs through limited analog channels, a CD74HC4067 multiplexer can be used. This allows sequential selection and routing of each sensor's output to a single analog pin on the micro-controller. The negative terminals of all sensors are connected together and grounded to the Arduino's ground, ensuring a unified reference. The micro controller powers an I2C-based LCD display using its 5 V output. Internally, the Arduino's 10-bit Analog-to-Digital Converter (ADC) is used to convert the analog signals into digital values. Since the voltage sensors reduce input voltage by a factor of five, the original voltages are calculated by multiplying the ADC results accordingly. The battery pack under observation consists of six series-connected strips, each made up of four lithium-ion cells in parallel, forming a 6S4P structure. Each cell is rated at 4 V and 2.6 Ah, giving the full pack a nominal voltage of 24 V and a capacity of 10.4 Ah. Voltage measurements across terminal points (from b_1-b_2 to b_1-b_7) yield values of 4 V, 8 V, 12 V, 16 V, 20 V, and 24 V respectively as shown in Fig. 6.1, confirming correct series configuration. The typical structure of the scaled down model of 6S4P LIB is shown in Fig. 6.1. The algorithm follows the flowchart shown in Fig. 4.1. The algorithm identifies a strip as abnormal if its voltage falls below a pre-defined threshold of 3.95 V, which is determined through experimental validation. Upon detection of a weak strip, an estimation equation is employed that incorporates the healthy cell voltage, the weak cell voltage, and the known contact resistance. If the estimated strip voltage aligns with the actual measured voltage within an acceptable threshold range, the system successfully determines the position of the weak cell within the strip.

6.3 Validation

The strip with the lowest voltage, particularly one falling below the 3.95 V threshold, is identified as the weak strip. As presented in Table 6.1, strips containing a weak cell consistently exhibit voltages below this threshold. Furthermore, within each weak strip, the corresponding weak cell demonstrates the highest temperature among all cells, thereby confirming thermal validation. Relative to the healthy condition, an increase in capacitance is also observed for weak cells. Capacitance is measured by injecting a 10 mV AC signal into the LIB, recording the resulting voltage and current using a digital oscilloscope, and applying the Discrete Fourier Transform (DFT) algorithm to extract the fundamental component of the impedance. The capacitance is then calculated from the derived impedance.

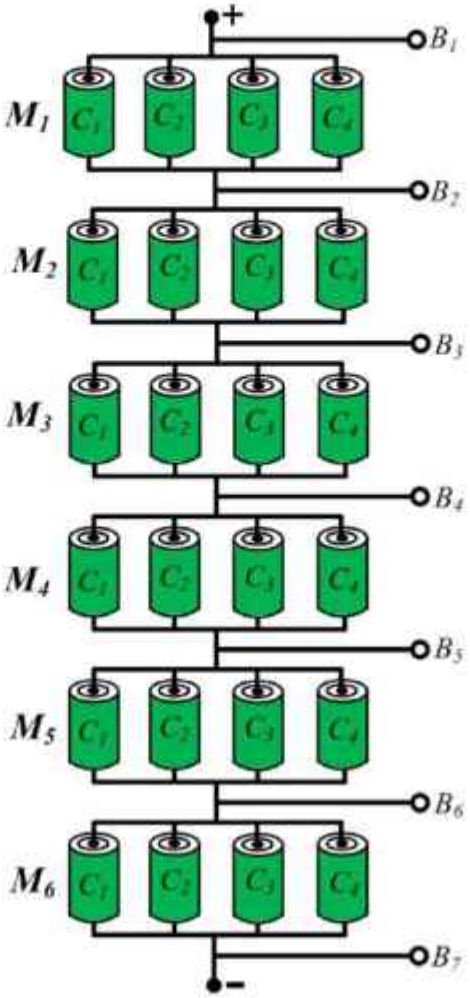

Figure 6.1: Typical structure of a scaled down model of a 6S4P LIB

Table 6.1: Thermal and Capacitance validation for weak cell detection

Case no	Particular weak location	Strip Voltages	T(°C)	% Change in Capacitance
1	Healthy	4.00, 4.00, 4.01, 4.02, 3.99, 4.00	33.2	0
2	S1C4	**3.85**, 4.00, 3.99, 4.01, 4.03, 4.00	36.6	5.05
3	S1C2	**3.87**, 3.99, 4.00, 4.01, 4.02, 4.00	35.4	6.13
4	S2C1	4.00, **3.91**, 4.01, 4.00, 3.99, 4.01	37.5	1.17
5	S2C3	4.00, **3.83**, 4.01, 3.99, 4.00, 4.03	36.2	4.6
6	S3C1	4.00, 3.99, **3.91**, 4.00, 4.01, 4.02	38.8	1.09
7	S3C4	4.01, 4.00, **3.83**, 4.02, 4.00, 4.00	37.1	0.57
8	S4C2	4.00, 3.99, 4.02, **3.89**, 4.02, 4.00	35.8	1.65
9	S4C3	4.01, 4.00, 4.02, **3.84**, 4.01, 4.01	36.8	1.23
10	S5C1	4.00, 4.00, 4.00, 4.01, **3.90**, 4.01	38.1	3.31
11	S5C2	4.00, 4.01, 4.00, 4.02, **3.88**, 4.00	35.9	2.51
12	S6C3	4.00, 4.00, 4.00, 3.99, 4.02, **3.81**	34.7	4.22
13	S6C4	4.01, 4.02, 4.00, 4.00, 4.01, **3.82**	36.0	2.86

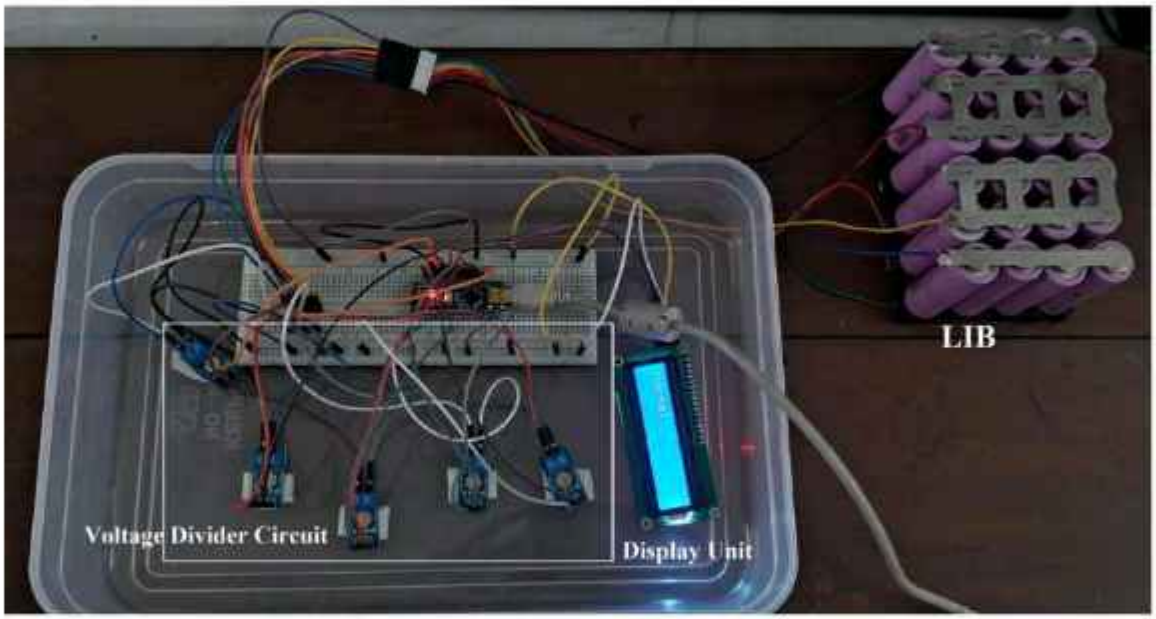

Figure 6.2: WAVES Setup

Figure 6.3: Validation by Capacitance method Setup

Chapter 7

Conclusion and Future Scope

This project introduces a novel method for identifying weak cell locations in LIB packs configured in a Multi-Series-N-Parallel (MSNP) arrangement. In this setup, cells connected in parallel are referred to as a strip or row. The method leverages strip voltage—influenced by both healthy and weak cells—as the primary indicator for detecting abnormalities.

Although contact resistance is generally low, its impact on strip voltage is non-negligible and is accounted for in the proposed model. A mathematical expression has been formulated that relates strip voltage to the voltages of healthy and weak cells, contact resistance, and pack configuration. Using this model and known cell voltages, the expected strip voltage can be estimated. If the measured strip voltage falls within ± 5 mV of the estimated value, the weak cell location is identified.

The equation incorporates weighted coefficients representing the N parallel-connected cells, allowing weak cell detection without requiring direct measurements of individual cell voltages or currents. This approach reduces the reliance on expensive sensors and intensive computation typically associated with conventional BMS.

Thermal validation is used to confirm the presence of weak cells. Due to elevated IR and reduced capacity, a weak cell heats up more than surrounding healthy cells, which supply charge to it. This charging effect leads to a drop in voltage and capacity of the healthy cells, reinforcing the detection of the weak cell.

The proposed method shows improved voltage and IR metrics for identified weak cells. Both MATLAB simulations and experimental tests confirm a consistent trend: strip voltage decreases as a weak cell is placed closer to the terminal end of the pack. Additionally, the study observes significant voltage shifts in individual cells when transitioning from isolated to parallel operation. Healthy cells lose voltage when connected to a weak cell, as it draws charge to equalize potential, thereby reducing overall strip voltage.

The developed WAVES (Weak cell Assessment using Voltage Estimation and Strip-data) technology enables real-time weak cell monitoring using strip voltage

data. This analytical approach relies on minimal parameters and does not require complex sensing. Strip voltage, an easily measurable parameter, can be monitored using simple voltage divider circuits coupled with high-resolution ADCs, which are integrated into the proposed system.

7.1 Future Scope

The current approach primarily addresses the detection of a single weak cell within a strip of a lithium-ion battery pack arranged in an MSNP (Multi-Series-N-Parallel) configuration. However, real-world battery systems often experience multiple cell degradations due to aging, manufacturing inconsistencies, or uneven operating conditions. As a result, future research will focus on extending the proposed methodology to identify multiple weak cells, whether located within the same strip or across different strips.

To achieve this, the analytical model will need to be enhanced to handle the combined voltage effects of several weak cells, while still maintaining low computational and sensing requirements. This may involve introducing pattern recognition techniques or machine learning algorithms capable of discerning complex voltage behaviors arising from multiple abnormal cells.

Moreover, the framework can be generalized for application in any MSNP battery architecture, making it adaptable to various pack sizes and configurations. Emphasis will also be placed on improving the system's real-time performance, robustness under dynamic load profiles, and integration with compact, low-cost hardware platforms.

In the long term, this methodology has the potential to support predictive diagnostics by tracking cell degradation trends over time, thus enabling early maintenance actions and improving the overall safety and reliability of battery-powered systems.

Bibliography

[1] M. Dubarry *et al.*, "Aging and failure mode diagnosis of EV batteries," *J. Power Sources*, vol. 196, no. 3, pp. 1033–1038, 2011.

[2] A. Barré *et al.*, "A review on lithium-ion battery aging mechanisms and estimations for automotive applications," *J. Power Sources*, vol. 241, pp. 680–689, 2013.

[3] J. Zhang and J. Lee, "A review on prognostics and health monitoring of Li-ion battery," *J. Power Sources*, vol. 196, no. 15, pp. 6007–6014, 2011.

[4] H. Eddahech *et al.*, "Thermal aging and safety performance of lithium-ion batteries," *Energy*, vol. 84, pp. 542–550, 2015.

[5] Y. Wang *et al.*, "State-of-charge estimation with adaptive Kalman filter for lithium batteries," *IEEE Trans. Ind. Electron.*, vol. 60, no. 12, pp. 5561–5571, 2013.

[6] S. Saxena *et al.*, "Quantifying EV battery end-of-life through analysis of travel needs with vehicle powertrain models," *J. Power Sources*, vol. 282, pp. 265–276, 2015.

[7] Z. Chen *et al.*, "Online cell fault diagnosis for lithium-ion battery packs using model-based methods," *IEEE Trans. Power Electron.*, vol. 34, no. 6, pp. 5713–5721, 2019.

[8] D. Andre *et al.*, "Characterization of high-power lithium-ion batteries by electrochemical impedance spectroscopy," *J. Power Sources*, vol. 196, no. 12, pp. 5349–5356, 2011.

[9] X. Feng *et al.*, "Thermal runaway mechanism of lithium-ion battery for electric vehicles: A review," *Energy Storage Mater.*, vol. 10, pp. 246–267, 2018.

[10] Y. Gao *et al.*, "Machine learning-enabled health prognostics for lithium-ion batteries," *Nature Energy*, vol. 5, no. 9, pp. 636–645, 2020.

[11] T. Kim *et al.*, "Balancing of a battery pack using cell current estimation," *IEEE Trans. Power Electron.*, vol. 27, no. 1, pp. 419–426, 2012.

[12] N. Omar *et al.*, "Lithium iron phosphate based battery – Assessment of the aging parameters and development of cycle life model," *Appl. Energy*, vol. 113, pp. 1575–1585, 2014.

[13] W. Waag, S. Käbitz, and D. U. Sauer, "Critical review of the methods for monitoring of lithium-ion batteries: The need for development of advanced state-of-charge estimation methods," *J. Power Sources*, vol. 226, pp. 76–91, 2013.

[14] X. Hu, C. Zou, C. Zhang, and Y. Li, "Technological developments in batteries: A survey on modern advances," *IEEE Trans. Ind. Informat.*, vol. 15, no. 4, pp. 2330–2345, 2019.

[15] Y. Xing, E. W. M. Ma, K. L. Tsui, and M. Pecht, "Battery management systems in electric and hybrid vehicles," *Energies*, vol. 4, no. 11, pp. 1840–1857, 2011.

[16] J. Zhang and J. Lee, "A review on prognostics and health monitoring of Li-ion battery," *J. Power Sources*, vol. 196, no. 15, pp. 6007–6014, 2011.

[17] M. Berecibar *et al.*, "Critical review of state-of-health estimation methods of Li-ion batteries for real applications," *Renew. Sustain. Energy Rev.*, vol. 56, pp. 572–587, 2016.

[18] A. Farmann *et al.*, "Critical review of on-board capacity estimation techniques for lithium-ion batteries in electric and hybrid electric vehicles," *J. Power Sources*, vol. 281, pp. 114–130, 2015.

[19] G. L. Plett, "Extended Kalman filtering for battery management systems of LiPB-based HEV battery packs—Part 1: Background," *J. Power Sources*, vol. 134, no. 2, pp. 252–261, 2004.

[20] C. Zhang *et al.*, "State-of-health estimation for Li-ion batteries by combining the incremental capacity analysis method with machine learning," *J. Energy Storage*, vol. 25, p. 100922, 2019.

[21] S. Xiong *et al.*, "Machine learning-based fault detection and prognosis of lithium-ion batteries: A critical review," *Energies*, vol. 13, no. 10, p. 2541, 2020.

[22] V. Jha and B. Krishnamurthy, "Modeling the SEI layer formation and its growth in lithium-ion batteries during charge-discharge cycling," *Ionics*, vol. 28, pp. 3661–3670, 2022.

[23] G. Luo, Y. Zhang, and A. Tang, "Capacity degradation and aging mechanisms evolution of lithium-ion batteries under different operation conditions," *Energies*, vol. 16, no. 10, p. 4232, 2023.

[24] T. M. Bandhauer, S. Garimella, and T. F. Fuller, "Critical review of thermal issues in lithium-ion batteries," *J. Electrochem. Soc.*, vol. 158, no. 3, pp. R1–R25, 2011.

[25] H. Maleki and J. N. Howard, "Thermal stability studies of Li-ion cells and components," *J. Electrochem. Soc.*, vol. 146, no. 9, pp. 3224–3229, 1999.

[26] Q. Wang *et al.*, "Thermal runaway caused fire and explosion of lithium-ion battery," *J. Power Sources*, vol. 208, pp. 210–224, 2012.

[27] N. S. Spinner *et al.*, "Advanced thermal management system for lithium-ion batteries," *Appl. Energy*, vol. 160, pp. 826–840, 2015.

[28] Z. Zhang *et al.*, "Novel flame-retardant electrolytes for lithium-ion batteries," *J. Am. Chem. Soc.*, vol. 136, no. 25, pp. 9058–9068, 2014.

[29] X. Huang *et al.*, "Thermal runaway prevention with ceramic separators," *Energy Environ. Sci.*, vol. 8, pp. 2344–2351, 2015.

[30] A. Pesaran *et al.*, *Battery thermal management for electric vehicles*. Golden, CO, USA: National Renewable Energy Laboratory, 2011.

[31] Z. Ling *et al.*, "Review on thermal management with phase change materials," *Renew. Sustain. Energy Rev.*, vol. 50, pp. 615–629, 2015.

[32] Z. Rao *et al.*, "Internal temperature sensing in Li-ion batteries," *J. Power Sources*, vol. 224, pp. 156–161, 2013.

[33] R. R. Richardson *et al.*, "Data-driven thermal runaway prediction," *Nat. Commun.*, vol. 11, p. 1, 2020.

[34] International Electrotechnical Commission, *IEC 62660: Secondary Li-ion cells for electric vehicles*, Geneva, Switzerland, 2018.

[35] S. S. Zhang, "A review on electrolyte additives for lithium-ion batteries," *J. Power Sources*, vol. 162, no. 2, pp. 1379–1394, 2006.

[36] P. Arora, R. E. White, and M. Doyle, "Capacity fade mechanisms and side reactions in lithium-ion batteries," *J. Electrochem. Soc.*, vol. 145, no. 10, pp. 3647–3667, 1998.

[37] Q. Wang *et al.*, "Thermal runaway caused fire and explosion of lithium-ion battery," *J. Power Sources*, vol. 208, pp. 210–224, 2012.

[38] R. Spotnitz and J. Franklin, "Abuse behavior of high-power, lithium-ion cells," *J. Power Sources*, vol. 113, no. 1, pp. 81–100, 2003.

[39] J. B. Goodenough and Y. Kim, "Challenges for rechargeable Li batteries," *Chem. Mater.*, vol. 22, no. 3, pp. 587–603, 2010.

[40] X. Zhang *et al.*, "Mechanical behavior of lithium-ion battery components," *J. Power Sources*, vol. 357, pp. 126–141, 2017.

[41] M. Sheikh *et al.*, "Impact mechanics of lithium-ion batteries," *Int. J. Impact Eng.*, vol. 133, p. 103334, 2019.

[42] L. Wang *et al.*, "In situ measurement of mechanical degradation in batteries," *Nat. Energy*, vol. 1, pp. 1–8, 2015.

[43] Deshpande, R., et al. (2012). Battery cycle life prediction with mechanical degradation models. *Journal of the Electrochemical Society*, **159**(10), A1730–A1738.

[44] Kermani, G., et al. (2018). Mechanical fatigue in battery electrodes. *Advanced Energy Materials*, **8**(24), 1801023.

[45] Liu, Y., et al. (2019). Stress-optimized silicon-graphite anodes. *ACS Nano*, **13**, 9036–9043.

[46] Xia, Y., et al. (2018). Crashworthy design of battery enclosures. *Thin-Walled Structures*, **132**, 822–832.

[47] Wierzbicki, T., et al. (2018). Crash analysis of battery packs with damping materials. *Journal of Power Sources*, **400**, 581–594.

[48] Hensel, J., et al. (2020). Precision manufacturing of battery electrodes. *Manufacturing Letters*, **24**, 17–20.

[49] Mueller, S., et al. (2021). Operando strain measurement in batteries. *Journal of Materials Chemistry A*, **9**, 12345–12356.

[50] Kermani, G., et al. (2022). Smart batteries with embedded stress sensors. *Advanced Materials*, **34**(15), 2107421.

[51] Sahraei, E., et al. (2014). Calibration of battery FEA models. *International Journal of Solids and Structures*, **51**(2), 311–321.

[52] Verdier, N., et al. (2020). Revisiting SEI decomposition kinetics. *Journal of The Electrochemical Society*, **167**(10), 100533.

[53] Soto, F. A., et al. (2018). Pressure evolution in Li-ion cells. *ACS Applied Materials & Interfaces*, **10**, 21307–21316.

[54] Jung, S.-K., et al. (2018). Cobalt dissolution mechanisms. *Energy & Environmental Science*, **11**, 1763–1769.

[55] Liu, T., et al. (2020). Metal crossover effects. *Nature Communications*, **11**, 1–12.

[56] Gmitter, A. J., et al. (2010). Hydrolysis of $LiPF_6$. *Journal of The Electrochemical Society*, **157**(3), A269–A274.

[57] Ravdel, B., et al. (2003). Thermal stability of electrolytes. *Journal of Power Sources*, **119**, 805–810.

[58] Shkrob, I. A., et al. (2014). Reduction mechanisms of additives. *The Journal of Physical Chemistry C*, **118**, 19661–19671.

[59] Chen, L., et al. (2018). Atomic layer deposition for cathodes. *Advanced Materials*, **30**(32), 1800938.

[60] Maurer, A., et al. (2019). Fluorinated electrolyte systems. *Chemical Communications*, **55**, 873–876.

[61] Schweidler, S., et al. (2020). Differential electrochemical mass spectrometry. *Journal of The Electrochemical Society*, **167**(10), 100511.

[62] Wang, Z., et al. (2021). Operando NMR of Li deposition. *Nature Nanotechnology*, **16**, 77–82.

[63] Liu, Y., et al. (2022). Machine learning for electrolyte design. *Science Advances*, **8**(15), eabj8184.

[64] Y. Liu and M. Chen, "Infrared thermography for non-contact thermal characterization of lithium-ion battery plates," *Int. J. Thermophys.*, vol. 43, no. 7, pp. 1–13, 2022.

[65] S. Bhaskar, R. Yadav, and P. Sharma, "Data-driven thermal anomaly detection in large-scale lithium-ion battery systems," *IEEE Trans. Ind. Informat.*, vol. 18, no. 9, pp. 6214–6223, Sep. 2022.

[66] Z. Tian, H. Zhao, and K. Wang, "Deep learning-based thermal fault localization in lithium-ion batteries using optimized mask R-CNN," *IEEE Access*, vol. 12, pp. 10492–10503, 2024.

[67] Z. Tian, H. Zhao, and Y. Sun, "Anti-interference thermal fault diagnosis in battery packs using autoencoder denoising networks," *IEEE Trans. Energy Convers, early access*, 2024.

[68] R. Singh, M. Gupta, and A. Rao, "Ultrasonic-based real-time monitoring and thermal runaway detection in lithium-ion batteries," *ACS Omega*, vol. 9, no. 3, pp. 2481–2491, 2024.

[69] Mitra, Desham, and Siddhartha Mukhopadhyay, "Detection and isolation of faults in a lithium-ion battery pack using a switched architecture of equivalent cell diagnosers," *Journal of Energy Storage* , vol. 90, 29 Apr. 2024, pp. 111811–111811.

[70] Li, Jinwen, Yunhong Che, Kai Zhang, Hongao Liu, Yi Zhuang, Congzhi Liu, and Xiaosong Hu, "Efficient Battery Fault Monitoring in Electric Vehicles: Advancing from Detection to Quantification," *Energy*,vol. 313, 8 Dec. 2024, p. 134150.

[71] Sepasiahooyi, Sara, and Farzaneh Abdollahi, "Fault Detection of New and Aged Lithium-Ion Battery Cells in Electric Vehicles," *Green Energy and Intelligent Transportation*,vol. 3, no. 3, June 2024, p. 100165.

[72] Liu, Qiquan, Jian Ma, Xuan Zhao, Kai Zhang, Kang Xiangli, and Dean Meng, "A novel method for fault diagnosis and type identification of cell voltage inconsistency in electric vehicles using weighted Euclidean distance evaluation and statistical analysis," *Energy*,vol. 293, 9 Feb. 2024, pp. 130575–130575

[73] Zhao, Jingyuan, Xuning Feng, Manh-Kien Tran, Michael Fowler, Minggao Ouyang, and Andrew F. Burke, "Battery Safety: Fault Diagnosis from Laboratory to Real World," *Journal of Power Sources*,vol. 598, 1 Apr. 2024, pp. 234111–234111.

[74] Zhao, Jingyuan, Xuning Feng, Manh-Kien Tran, Michael Fowler, Minggao Ouyang, and Andrew F. Burke, "Fault Detection and Isolation in EV Battery Using Machine Learning Approach.," *2022 8th International Conference*

on Advanced Computing and Communication Systems (ICACCS),14 Mar. 2024, pp. 729–734.

[75] A. Shufian, N. Hannan, M. M. H. Emon, S. Kabir, S. A. Fattah, and M. S. Hossain, "Automatic fault detection and analysis of electric vehicle charging station by machine learning," in *Proc. IEEE Region 10 Symp. (TENSYMP)*, 2024, pp. 1–6.

[76] M. B. Kaleem, Y. Zhou, F. Jiang, Z. Liu, and H. Li, "Fault detection for Li-ion batteries of electric vehicles with segmented regression method," *Sci. Rep.*, vol. 14, no. 1, pp. Article 82960, Apr. 2024. Accessed on: May 2, 2025, DOI: 10.1038/s41598-024-82960-0.

[77] A. Singh, A. Lodge, Y. Li, W. D. Widanage, and A. Barai, "A new method to perform Lithium-ion battery pack fault diagnostics – Part 2: Algorithm performance in real-world scenarios and cell-to-cell transferability," *Energy Rep.*, vol. 11, pp. 304–315, Nov. 2023. Accessed on: May 2, 2025, DOI: 10.1016/j.egyr.2023.11.057.

[78] L. Ma, B. Duan, C. Zhang, Y. Kang, C. Li, and K. Liu, "Detection and differentiation of multiple types of minor anomalies in battery packs," *Energy*, vol. 2025, Art. no. 135557, Apr. 2025. Accessed on: May 2, 2025, DOI: 10.1016/j.energy.2025.135557.

[79] J. Hong, F. Liang, J. Yang, and S. Du, "An exhaustive review of battery faults and diagnostic techniques for real-world electric vehicle safety," *J. Energy Storage*, vol. 99, Art. no. 113234, Mar. 2024. Accessed on: May 2, 2025, DOI: 10.1016/j.est.2024.113234.

[80] S. Park, B. Kang, D. Yu, M. Jeong, and Y. Hong, "Fault diagnosis for electric vehicle battery pack interconnection system using real-world driving data," *IEEE Trans. Ind. Electron.*, pp. 1–9, Jan. 2025. Accessed on: May 2, 2025, DOI: 10.1109/TIE.2024.3522461.

[81] X. Peng, S. Duan, C. Sankavaram, and X. Jin, "Unsupervised adaptive fleet battery pack fault detection with concept drift under evolving environment," *IEEE Trans. Autom. Sci. Eng.*, vol. 21, no. 3, pp. 2276–2288, Jul. 2024. Accessed on: May 2, 2025, DOI: 10.1109/TASE.2024.3363002.

[82] D. H. Avinash and A. Rammohan, "Integrating level shift anomaly detection for fault diagnosis of battery management system for Lithium-Ion batteries,"

IEEE Access, vol. 12, pp. 116071–116084, 2024. Accessed on: May 2, 2025, DOI: 10.1109/ACCESS.2024.3445955.

[83] K. Bhaskar, A. Kumar, J. Bunce, J. Pressman, N. Burkell, N. Miller, and C. D. Rahn, "Faulty sensor signal reconstruction in Li-ion battery packs," *IEEE Trans. Transp. Electrific.*, vol. 11, no. 1, pp. 359–368, Mar. 2024. Accessed on: May 2, 2025, DOI: 10.1109/TTE.2024.3390652.

[84] S. Wang, Z. Wang, J. Pan, Z. Zhang, and X. Cheng, "Data-driven fault tracing of lithium-ion batteries in electric vehicles," *IEEE Trans. Power Electron.*, vol. 39, no. 12, pp. 16609–16621, Dec. 2024. Accessed on: May 2, 2025, DOI: 10.1109/TPEL.2024.3441572.

[85] D. Qiao, X. Wei, B. Jiang, W. Fan, H. Gong, X. Lai, Y. Zheng, and H. Dai, "Data-driven fault diagnosis of internal short circuit for series-connected battery packs using partial voltage curves," *IEEE Trans. Ind. Informat.*, vol. 20, no. 4, pp. 6751–6761, Apr. 2024. Accessed on: May 2, 2025, DOI: 10.1109/TII.2024.3353872.

[86] H. Jin, Z. Zhang, S. X. Ding, Z. Gao, Y. Wang, and Z. Zuo, "Fault diagnosis for parallel lithium-ion battery packs with main current sensor fault and internal resistance fault," *IEEE Trans. Instrum. Meas.*, vol. 73, pp. 1–10, 2024. Accessed on: May 2, 2025, DOI: 10.1109/TIM.2024.3400362.

[87] Y. Xu, X. Ge, R. Guo, C. Hu, and W. Shen, "Electrode-parameter-based fault diagnosis and capacity estimation for lithium-ion batteries in electric vehicles," *IEEE Trans. Ind. Electron.*, pp. 1–11, 2024. Accessed on: May 2, 2025, DOI: 10.1109/TIE.2024.3447749.

[88] A. Tang, Z. Wu, Y. Xu, K. Liu, and Q. Yu, "Cloud-based Li-ion battery anomaly detection, localization and classification," *IEEE Trans. Ind. Informat.*, pp. 1–9, 2024. Accessed on: May 2, 2025, DOI: 10.1109/TII.2024.3514131.

[89] F. Peng, S. Jiang, Y. Zhao, and L. Ren, "Soft short-circuit fault diagnosis for vehicular battery packs with interpretable full-dimensional statistical analytics," *IEEE Trans. Power Electron.*, vol. 39, no. 9, pp. 11650–11664, Sep. 2024. Accessed on: May 2, 2025, DOI: 10.1109/TPEL.2024.3404962.

[90] X. Zhao, J. Wang, M. Zhao, B. Pan, R. Wang, L. Wang, and X. Yan, "Micro-short circuit fault diagnosis of the parallel battery module based on increment capacity curve," *J. Energy Storage*, vol. 86, Art. no. 111201, 2024. Accessed on: May 2, 2025, DOI: 10.1016/j.est.2024.111201.

[91] L. Torres-Castro, A. M. Bates, N. B. Johnson, G. Quintana, and L. Gray, "Early detection of Li-ion battery thermal runaway using commercial diagnostic technologies," *J. Electrochem. Soc.*, vol. 171, no. 2, Art. no. 020520, 2024. Accessed on: May 2, 2025, DOI: 10.1149/1945-7111/ad2440.

[92] D. Qiao, X. Wei, B. Jiang, W. Fan, X. Lai, Y. Zheng, and H. Dai, "Quantitative diagnosis of internal short circuit for lithium-ion batteries using relaxation voltage," *IEEE Trans. Ind. Electron.*, vol. 71, no. 10, pp. 13201–13210, Oct. 2024. Accessed on: May 2, 2025, DOI: 10.1109/TIE.2023.3342289.

[93] M. B. Kaleem, Y. Zhou, F. Jiang, Z. Liu, and H. Li, "Fault detection for Li-ion batteries of electric vehicles with segmented regression method," *Sci. Rep.*, vol. 14, no. 1, 2024. Accessed on: May 2, 2025, DOI: 10.1038/s41598-024-82960-0.

[94] N. Zhou, K. Wang, X. Shi, and Z. Chen, "Detection and analysis of abnormal high-current discharge of cylindrical lithium-ion battery based on acoustic characteristics research," *World Electric Vehicle J.*, vol. 15, no. 6, Art. no. 229, 2024. Accessed on: May 2, 2025, DOI: 10.3390/WEVJ15060229.

[95] M. Wu, S. Zhang, F. Zhang, R. Sun, J. Tang, and S. Hu, "Anomaly detection method for lithium-ion battery cells based on time series decomposition and improved Manhattan distance algorithm," *ACS Omega*, vol. 9, no. 2, pp. 2409–2421, 2023. Accessed on: May 2, 2025, DOI: 10.1021/acsomega.3c06796.

[96] J. N. E. Lucero, V. A. Sujan, and S. Onori, "An experimentally validated electro-thermal EV battery pack model incorporating cycle-life aging and cell-to-cell variations," *IEEE Trans. Transp. Electrific.*, vol. 1, 2024. Accessed on: May 2, 2025, DOI: 10.1109/TTE.2024.3365028.

[97] S. K. Pradhan and B. Chakraborty, "Battery management strategies: An essential review for battery state of health monitoring techniques," *J. Energy Storage*, vol. 51, Art. no. 104427, 2022. Accessed on: May 2, 2025, DOI: 10.1016/j.est.2022.104427.

[98] V. Azimi, A. Allam, and S. Onori, "Extending life of lithium-ion battery systems by embracing heterogeneities via an optimal control-based active balancing strategy," *IEEE Trans. Control Syst. Technol.*, vol. 31, no. 3, pp. 1235–1249, May 2023. Accessed on: May 2, 2025, DOI: 10.1109/TCST.2022.3215610.

Appendix A

Code for DFT

```
clear , clc
fsig = 100;
N = 1000;
fs = 10;
dt = 1/fs;
x = xlsread('tek00XX.csv', 'Ya:Yb');
for m = 0:N-1
X(m+1) = 0;
end
for m = 0:N-1
for n = 0:N-1
X(m+1) = X(m+1) + x(n+1) * exp(-j*2*pi*m*n/N);
end
end
X_DFT = fft(x);
for m = 0:N-1
DFT_Error(m+1) = abs(X(m+1) - X_DFT(m+1));
end
max_error = max(DFT_Error);
for m = 0:N-1
m+1;
real(X(m+1));
imag(X(m+1));
m+1;
real(X_DFT(m+1));
imag(X_DFT(m+1));
end
a0_calc = X_DFT(1)/N;
```

```
a1_calc = real(X_DFT(2)*(2/N));
b1_calc = -imag(X_DFT(2)*(2/N));
a2_calc = real(X_DFT(3)*(2/N));
b2_calc = -imag(X_DFT(3)*(2/N));
a3_calc = real(X_DFT(4)*(2/N));
b3_calc = -imag(X_DFT(4)*(2/N));
a4_calc = real(X_DFT(5)*(2/N));
b4_calc = -imag(X_DFT(5)*(2/N));
a5_calc = real(X_DFT(6)*(2/N));
b5_calc = -imag(X_DFT(6)*(2/N));
a6_calc = real(X_DFT(7)*(2/N));
b6_calc = -imag(X_DFT(7)*(2/N));
a7_calc = real(X_DFT(8)*(2/N));
b7_calc = -imag(X_DFT(8)*(2/N));
a8_calc = real(X_DFT(9)*(2/N));
b8_calc = -imag(X_DFT(9)*(2/N));
a9_calc = real(X_DFT(10)*(2/N));
b9_calc = -imag(X_DFT(10)*(2/N));
a10_calc = real(X_DFT(11)*(2/N));
b10_calc = -imag(X_DFT(11)*(2/N));
a11_calc = real(X_DFT(12)*(2/N));
b11_calc = -imag(X_DFT(12)*(2/N));
a12_calc = real(X_DFT(13)*(2/N));
b12_calc = -imag(X_DFT(13)*(2/N));
a13_calc = real(X_DFT(14)*(2/N));
b13_calc = -imag(X_DFT(14)*(2/N));
a14_calc = real(X_DFT(15)*(2/N));
b14_calc = -imag(X_DFT(15)*(2/N));
a15_calc = real(X_DFT(16)*(2/N));
b15_calc = -imag(X_DFT(16)*(2/N));
m1 = abs(a1_calc + j*b1_calc);
m2 = abs(a2_calc + j*b2_calc);
m3 = abs(a3_calc + j*b3_calc);
m4 = abs(a4_calc + j*b4_calc);
m5 = abs(a5_calc + j*b5_calc);
m6 = abs(a6_calc + j*b6_calc);
m7 = abs(a7_calc + j*b7_calc);
m8 = abs(a8_calc + j*b8_calc);
```

```
m9 = abs(a9_calc + j*b9_calc);
m10 = abs(a10_calc + j*b10_calc);
m11 = abs(a11_calc + j*b11_calc);
m12 = abs(a12_calc + j*b12_calc);
m13 = abs(a13_calc + j*b13_calc);
m14 = abs(a14_calc + j*b14_calc);
m15 = abs(a15_calc + j*b15_calc);
p1 = atan(b1_calc/a1_calc)*(180/3.1415);
p2 = atan(b2_calc/a2_calc)*(180/3.1415);
p3 = atan(b3_calc/a3_calc)*(180/3.1415);
p4 = atan(b4_calc/a4_calc)*(180/3.1415);
p5 = atan(b5_calc/a5_calc)*(180/3.1415);
p6 = atan(b6_calc/a6_calc)*(180/3.1415);
p7 = atan(b7_calc/a7_calc)*(180/3.1415);
p8 = atan(b8_calc/a8_calc)*(180/3.1415);
p9 = atan(b9_calc/a9_calc)*(180/3.1415);
p10 = atan(b10_calc/a10_calc)*(180/3.1415);
p11 = atan(b11_calc/a11_calc)*(180/3.1415);
p12 = atan(b12_calc/a12_calc)*(180/3.1415);
p13 = atan(b13_calc/a13_calc)*(180/3.1415);
p14 = atan(b14_calc/a14_calc)*(180/3.1415);
p15 = atan(b15_calc/a15_calc)*(180/3.1415);
```